

# **The Role of Cloud-Radiative Interaction in Tropical Circulation and the Madden-Julian Oscillation**

Yuanyuan Huang<sup>a</sup>, Daehyun Kim<sup>b,c</sup>, Tian Zhou<sup>d</sup>, Xiaoming Shi<sup>a,e</sup>

<sup>a</sup> *Division of Environment and Sustainability, The Hong Kong University of Science and  
Technology, Hong Kong, China*

<sup>b</sup> *School of Earth and Environmental Sciences, Seoul National University, Seoul, South Korea*

<sup>c</sup> *Department of Atmospheric Sciences, University of Washington, Seattle, WA, USA*

<sup>d</sup> *College of Atmospheric Sciences, Lanzhou University, Lanzhou, Gansu, China*

<sup>e</sup> *Center for Ocean Research in Hong Kong and Macau, The Hong Kong University of Science  
and Technology, Hong Kong, China*

*Corresponding author: Xiaoming Shi, shixm@ust.hk*

12 ABSTRACT: Cloud-radiative interaction (CRI) is a fundamental process that modulates tropical  
13 circulation and intraseasonal variability, including the Madden-Julian Oscillation (MJO). In this  
14 study, we investigate how the mean state of the tropical atmosphere and MJO respond to CRI  
15 intensity changes and provide insights into the underlying mechanisms, using the aquaplanet  
16 configuration in CESM2. By enhancing CRI through tuning the DCS parameter (an auto-conversion  
17 threshold size in Morrison and Gettelman (2008) cloud microphysics scheme), we demonstrate that  
18 DCS-induced CRI intensification is linked to a warmer troposphere, increased tropical moisture,  
19 strengthened Hadley Cell (HC), stronger trade winds, and a stronger equatorward intertropical  
20 convergence zone (ITCZ) with more clouds and precipitation, reflecting stronger cloud-radiation-  
21 circulation feedback. The intensified CRI also leads to the intensification and slower propagation  
22 of the simulated MJO-like mode despite the MJO-like signals becoming less distinguishable from  
23 the background due to the influence of other waves. The MJO intensification is likely associated  
24 with the mean state changes that support the development of deep convection. Moreover, the CRI  
25 itself, especially the interaction with the longwave radiation, also directly influences the MJO's  
26 maintenance and propagation, more contributing to the maintenance of column moist static energy  
27 (MSE) and deceleration of its eastward propagation on intraseasonal timescales.

## 1. Introduction

Cloud-radiative interaction (CRI) is a broad definition of a dynamic and complex process in the Earth's atmosphere, involving a complex interplay between cloud properties and the radiation budget. The level, thickness, distribution, and other internal properties of clouds interact with the shortwave (SW) solar radiation and the longwave (LW) radiation emitted by the Earth, producing distinct radiative feedback to the atmosphere. CRI is usually recognized for its great importance in regulating global-scale atmospheric circulation and diverse climate or weather events through different dynamics and thermodynamics processes (e.g., Tao et al. 1996; Tian and Ramanathan 2003; Ceppi et al. 2014; Ceppi and Hartmann 2015; Li et al. 2015; Shaw 2019; Zhang et al. 2021). The concept of CRI is analogous to the cloud-radiative feedback.

Although the large-scale circulations in higher latitudes can be significantly affected by CRI changes, such as subtropical jet shift and intensification (e.g., Li et al. 2015; Shaw 2019), the tropical atmosphere appears to be more susceptible to the CRI changes because net energy input to the global climate system and concentrated water vapor always colocate at the low latitudes, leading to frequent deep convection and extensive cloud coverage. Tropical extreme precipitation has been proven to be greatly influenced by CRI (e.g., Medeiros et al. 2021; Zhang et al. 2021). Zhang et al. (2021) also highlight the role of CRI in the spatial organization of convection and find that the convective aggregation is reduced when the synoptic variabilities of CRI are disabled. Apart from the extreme events and aggregated convection, the responses of the tropical mean precipitation and circulations to the presence or the changes of CRI are also paid high attention. For example, Tian and Ramanathan (2003) suggest that CRI drives and maintains the Hadley and Walker circulations via a moist dynamic model. Harrop and Hartmann (2016) mainly focus on the tropical changes using the Clouds On-Off Klimate Intercomparison Experiment (COOKIE) and find that when CRI is turned on, the Hadley Cell (HC) strengthens, the intertropical convergence zone (ITCZ) contracts toward the equator with higher values of precipitation, and the tropical atmosphere is moistened.

Other smaller-scale atmospheric processes and systems in the tropics are also controlled by CRI variation. These atmospheric processes and systems are often convectively coupled, in which the CRI plays its salient role through deep convective clusters and clouds. Many previous studies have highlighted the role of CRI in modulating the Madden-Julian Oscillation (MJO), a representative of convectively coupled tropical intraseasonal variability, first discovered by Madden

58 and Julian (1971). Various studies of CRI effects on MJO focusing on different perspectives provide  
59 theoretical and technical bases for a better understanding of MJO as well as better MJO simulations  
60 and predictions.

61 Some of those studies diagnose and analyze the CRI-MJO relationship based on the observations.  
62 For example, Zhang et al. (2019) suggest that the CRI shows its strongest feedback to MJO compared  
63 to other radiative components (e.g, water vapor feedback) and the stronger CRI associated with  
64 MJO helps the MJO propagate eastward surviving the barrier effect of the Maritime Continent.  
65 Kim et al. (2015) define a greenhouse enhancement factor (GEF) to measure CRI at different MJO  
66 stages and find a positive correlation between the GEF strength and climate models' fidelity in  
67 simulating the MJO.

68 Some other studies focus on the CRI-MJO performance in the numerical models by conducting  
69 denial experiments or comparing the different simulation datasets. Hu et al. (2022) show the MJO  
70 is absent in simulations without cloud-radiative effect. Crueger and Stevens (2015) select four  
71 coupled climate models in COOKIE which makes clouds transparent to radiation to eliminate the  
72 radiative effects on the clouds. Their findings suggest that turning on the CRI leads to stronger  
73 MJO and slower propagation. Shi et al. (2018) control the LW CRI effects by prescribing zonally  
74 uniform LW heating rate. Their results show that enabling the CRI variabilities can influence the  
75 scale selection of MJO by strengthening low-wavenumber modes but CRI does not determine the  
76 formation of MJO. Benedict et al. (2020) use the "cloud locking" method to isolate CRI impacts on  
77 MJO and minimize the mean state change, showing that the disabled CRI suppresses the MJO and  
78 the larger-wavenumber features, consistent with the results of Crueger and Stevens (2015) and Shi  
79 et al. (2018) for MJO strength, while contrary to the results of scale selection in Shi et al. (2018).

80 The differences in simulation results about the impacts of CRI on MJO across various studies  
81 might be attributed to model- or method-dependency, but they could also arise from the climate  
82 system's complexity. Therefore, understanding how CRI affects MJO behavior and how it can  
83 be accurately represented in numerical models to improve the MJO simulation performance re-  
84 mains a pressing and popular topic, requiring further support from experiments and theoretical  
85 investigations.

86 In this study, we intend to investigate how CRI modulates tropical mean circulation and MJO  
87 using idealized aquaplanet simulations. The simpler aquaplanet model is often regarded as a

88 useful idealization not only for studying global general circulation but also for studying tropical  
89 intraseasonal oscillations (Lee et al. 2001; Maloney et al. 2010; Leroux et al. 2016; Shi et al.  
90 2018; Andersen and Kuang 2012). It provides an ocean-only lower boundary condition with  
91 fixed sea surface temperature (SST) which avoids the CRI effect on mean circulation and MJO  
92 being influenced by some complex processes, such as land-sea distribution and variable SST  
93 patterns. Furthermore, we control the CRI intensity with a smoother transition by tuning a  
94 sensitive cloud microphysics parameter, which sets our experiments apart from those CRI “on-off”  
95 experiments, like COOKIE (Li et al. 2015; Harrop and Hartmann 2016) and “cloud locking”  
96 (Benedict et al. 2020), or the removal of the CRI spatial-temporal variabilities by zonally uniform  
97 radiation prescribing (Lee et al. 2001; Shi et al. 2018).

98 In addition, according to the previous research, the changes in HC, equatorial wind, tropical  
99 moisture, and the moisture gradient are all regarded as crucial factors affecting MJO behaviors  
100 (e.g., Adames and Wallace 2015; Crueger and Stevens 2015; Kang et al. 2021; Rushley et al. 2023).  
101 For example, the mean state with stronger HC caused by the changes in Earth orbit parameters  
102 increases the MJO precipitation variance (Rushley et al. 2023), and the larger meridional moisture  
103 gradient may enhance the MJO propagation over the Maritime Continent in boreal winter (Kang  
104 et al. 2021). Nevertheless, given that the CRI changes can influence the mean circulation and MJO,  
105 it raises the question of whether alterations in mean circulation can serve as a linkage between CRI  
106 changes and MJO variability. We will further explore this question based on our simulations and  
107 attempt to explain the underlying physical mechanisms.

108 This manuscript is organized as follows. Section 2 describes the model and parameter details  
109 of our simulations as well as the MJO analysis method. Section 3 describes the climate mean  
110 state changes under the intensified CRI. Section 4 describes the MJO characteristic changes in our  
111 simulations and discusses the possible mechanisms of MJO changes. The summary of our results  
112 and further discussion follow in Section 5.

## 113 **2. Model and Methods**

### 114 *a. Aquaplanet Model*

115 In our study, we use the atmospheric component of Community Earth System Model version  
116 2 (CESM2), Community Atmosphere Model version 6 (CAM6, Bogenschutz et al. 2018). The

117 aquaplanet configuration is applied to make CAM6 run above the prescribed zonally uniform SST  
 118 based on the Aqua-Planet Experiment (APE, Williamson et al. 2012). The SST pattern is the  
 119 “QOBS”, as defined in the APE. The maximum SST is 27 °C at the equator. The SST decreases  
 120 gradually with latitude and is maintained at 0 °C between 60° and 90° in both hemispheres:

$$T(\phi) = \begin{cases} \frac{1}{2} (2 - \sin^4 \varphi - \sin^2 \varphi) \delta T + T_{\min}, & \text{if } |\phi| < \frac{\pi}{3} \\ 0, & \text{otherwise} \end{cases}, \quad (1)$$

121 where  $\phi$  is latitude,  $\varphi = \frac{\pi}{2} \frac{\phi}{\phi_{\max}}$ ,  $\phi_{\max} = \frac{\pi}{3}$ ,  $\delta T = T_{\max} - T_{\min}$ ,  $T_{\max} = 27$  °C,  $T_{\min} = 0$  °C. The SST  
 122 distribution and meridional profile are shown in Figure 1.

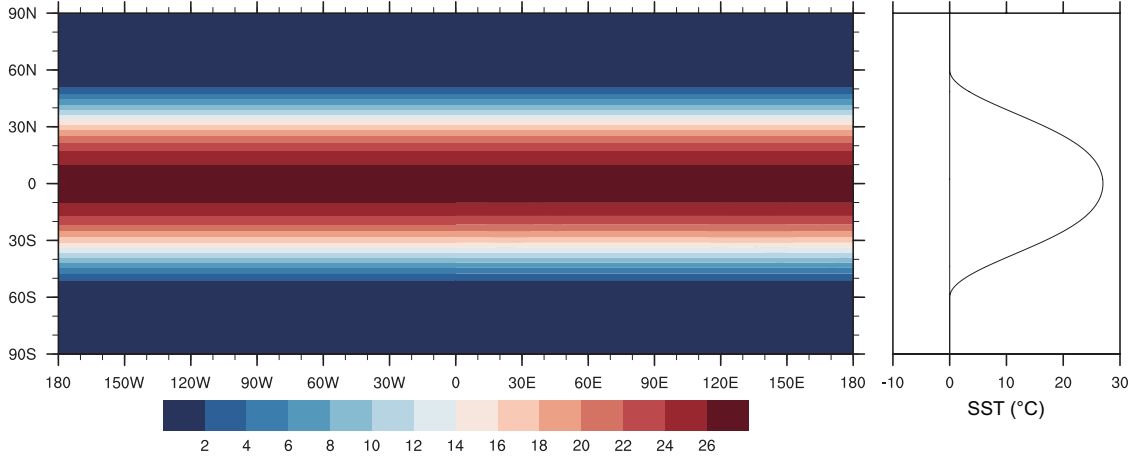


FIG. 1. SST global distribution and meridional profile (units: °C).

123 The mean state simulated by such configurations is possibly different from that in the real world,  
 124 especially the zonal-uniform and hemisphere-symmetric “QOBS” SST pattern without Warm Pool  
 125 and the cross-equatorial flow induced by cross-equatorial SST gradient. For example, over the  
 126 Warm Pool, the mean low-level zonal wind shows a dominant westerly component, opposite to the  
 127 easterlies in other tropical regions. The mean state wind in our simulations does not seem like that,  
 128 which will be discussed in Section 3a. The aquaplanet configuration with “QOBS” SST reflects its  
 129 limitation but meets our research purpose which focuses on the more intrinsic CRI impart without  
 130 the influence of Warm Pool and cross-equator flow. Nonetheless, it is still necessary to note this  
 131 issue, especially when comparing the differences between our simulations and the observations.

132 The default CAM6 aquaplanet adopts a finite volume (FV) dynamical core on a latitude-longitude  
133 grid with a horizontal resolution of  $0.9^\circ$  latitude  $\times$   $1.25^\circ$  longitude and 32 hybrid sigma-pressure  
134 levels. The model uses Cloud Layers Unified by Binormals (CLUBB, Golaz et al. 2002; Larson  
135 et al. 2002) scheme to parameterize the boundary layer, turbulence, shallow convection, and cloud  
136 macrophysics. The Zhang and McFarlane (1995) deep convection scheme and the Gettelman and  
137 Morrison (2015) cloud microphysics scheme are also adopted in the model. The radiative transfer  
138 is represented by the Rapid Radiative Transfer Model for General Circulation Models (RRTMG,  
139 Iacono et al. 2008). More aquaplanet-related details are documented in Medeiros et al. (2016).

#### 140 *b. DCS and Experiment Design*

141 DCS refers to the auto-conversion threshold size defined in Equations (29) and (30) in Morrison  
142 and Gettelman (2008). In this cloud microphysics scheme, cloud ice and snow are separated into  
143 two categories. The DCS value determines when the auto-conversion from ice to snow takes place  
144 in numerical calculations. Smaller DCS values result in a more efficient conversion of cloud ice  
145 into snow, reducing the cloud ice. In contrast, larger DCS delays this conversion until the cloud  
146 ice particles grow to a larger size, causing more cloud ice to remain in the atmosphere. DCS is  
147 considered an effective turning parameter not only for tuning the model to reach its energy balance  
148 but also for investigating the specific scientific questions related to the cloud-radiative feedback  
149 (Zhao et al. 2013; Fan et al. 2021). The high sensitivity of cloud-radiative feedback to DCS has  
150 been demonstrated by Zhao et al. (2013), Eidhammer et al. (2014), and Pathak et al. (2020).

151 In this study, three main experiments are conducted by setting different DCS values in the CESM2  
152 aquaplanet model. The default DCS value for CESM2 aquaplanet configuration is  $500\text{ }\mu\text{m}$ , and  
153 the DCS values are set to  $200\text{ }\mu\text{m}$  and  $800\text{ }\mu\text{m}$  in two additional experiments. We name the three  
154 experiments DCS200, DCS500, and DCS800, respectively. All three experiments are integrated  
155 for ten years, with the first two-year simulation data discarded as spin-up, the last eight-year data  
156 considered as the stable state and used for analysis. The data are archived once a day.

#### 157 *c. CRI and Cloud Forcing*

158 The concept of CRI in this manuscript is a broad definition, rather than a metric of a certain  
159 quantity. For example, some studies define a cloud-radiative feedback parameter to represent the

role of CRI, which is often used in linear analytical models, such as Fuchs and Raymond (2002), Fuchs and Raymond (2005), Sobel and Maloney (2012), and Fuchs-Stone (2020).

In this study, we tune the DCS parameter to control the CRI intensity with a smoother transition, unlike the CRI “on-off” experiments. We suggest that the smaller DCS causes the weaker CRI due to less cloud ice in the atmosphere, while stronger CRI is associated with larger DCS since more cloud ice has a stronger interaction with radiation.

Our method (tuning DCS) causes changes in CRI itself and the mean state. The mean convection changes (discussed in Section 3) are not a direct result of the cloud microphysics change, but an indirect result of the large-scale circulation’s thermodynamics and dynamics adjustment in response to the CRI intensity change.

We only care about the radiative effect on the atmosphere (not on the whole earth system or the surface) associated with clouds in this study. In some other studies, they also call it the atmospheric cloud-radiative effect (ACRE). When investigating the representation of CRI intensity, we calculate the cloud radiative forcing (hereafter called cloud forcing). The cloud forcing is calculated as the difference of column radiative convergence (the difference between net radiation flux at the top of the atmosphere and that at the surface) between the clearsky and cloudy conditions. The calculation of cloud forcing is considered the sum of the SW and LW components in order to present the total cloud-radiative effect, though the LW component is the main contributor to the total CRI.

#### *d. MJO-Associated Regression*

The linear regression method (Adames and Wallace 2014a, 2015) is applied to analyze the spatial structure of MJO-like disturbances, and the equation is as follows:

$$\mathbf{D} = \mathbf{S}\hat{\mathbf{P}}^T/N \quad (2)$$

where  $\mathbf{D}$  is the regression results with the dimensional units,  $\mathbf{S}$  is a two-dimensional matrix of the variable  $S$ ,  $\hat{\mathbf{P}}$  is the time series of the MJO index,  $N$  is the sample size of the daily archived variable  $S$ , and the superscript  $T$  represents the transposition of a matrix.

The MJO index is calculated as follows: we select an approximate  $5^\circ \times 5^\circ$  square box of precipitation rate centered at  $180^\circ$  on the equator. Then, we spatially average the precipitation rate



186 in this region and standardize the resulting time series. A 20 to 100-day bandpass filter is also  
187 applied.

### 188 **3. CRI-Induced Mean State Changes**

#### 189 *a. Climate Mean State*

190 Through tuning DCS in the CESM2 aquaplanet model, the climate mean state, including the  
191 thermodynamic conditions and large-scale circulations, presents discernible changes in the time-  
192 and-zonal-averaged plots. In this study, we mainly discuss those changes in the tropical atmosphere.

200 The air temperature changes with DCS are shown in the upper row of Figure 2. When DCS  
201 is tuned larger, the tropical tropospheric temperature significantly increases, particularly in the  
202 upper troposphere (around 300-hPa) and the height of tropical tropopause becomes higher. Such  
203 tropospheric warming may be attributed to the enhanced condensational heating and radiative  
204 heating and we will further discuss it in the following text. The tropical warming also leads to  
205 a larger temperature meridional gradient, driving a stronger poleward meridional heat transport.  
206 This warming pattern shares some similarities with greenhouse gas-caused warming in that the  
207 upper troposphere warms faster than the lower troposphere.

208 Figure 2d-f show the fractional changes of moisture with DCS. The moisture amount generally  
209 expands with increasing DCS in the deep tropics, especially having larger fractional changes in the  
210 middle and higher troposphere. It means that more moisture transports upward from the boundary  
211 layer to the higher altitudes and converges therein. We also notice that there is a moisture decrease  
212 between 10°S/N–30°S/N outside the deep tropics, enhancing the meridional moisture gradient  
213 between deep tropics and subtropics.

218 Figure 3 depicts the time-mean, zonal-mean meridional mass stream function (MMSF), cloud  
219 fraction, and zonal wind with varying DCS values. As DCS increases, more cloud ice in the  
220 tropical atmosphere leads to a larger cloud fraction (the left column of Figure 3), particularly in the  
221 middle and upper troposphere. Concurrently, the positive/negative MMSF in the lower latitudes  
222 of the Northern/Southern Hemisphere (NH/SH) intensifies with increasing DCS, reflecting the  
223 strengthening of the HC. The changes in HC also explain the moisture distribution change in  
224 Figure 2d–f. The deep tropics moistening is due to the strengthening of the ascending branch of the

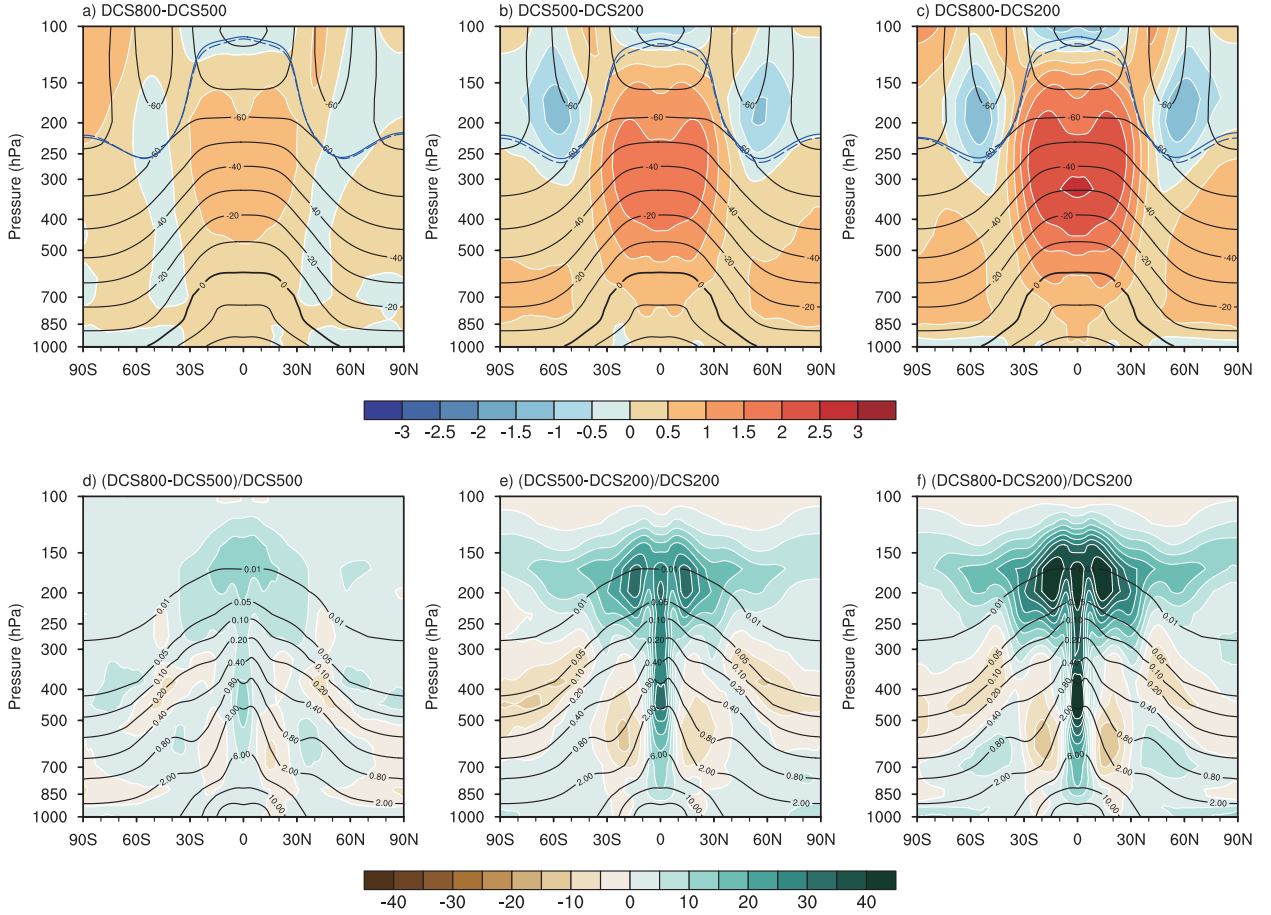


FIG. 2. (a, b, c) The changes of climatological zonal-averaged air temperature (color, units:  $^{\circ}\text{C}$ ) and (d, e, f) the fractional changes of climatological zonal-averaged specific humidity (color, units:  $\%$ ) between different cases. The climatological zonal-averaged air temperature and specific humidity of the DCS500 case are plotted as a reference (contour, units:  $^{\circ}\text{C}$  for air temperature and  $\text{g/kg}$  for specific humidity). The interval of temperature contour is  $10^{\circ}\text{C}$  and the interval of specific humidity contour is not evenly spaced (0.01, 0.05, 0.1, 0.2, 0.4, 0.8, 2, 6, 10, 14). The overlaid blue curves in the upper row represent the height of the tropopause. The blue solid curves are calculated in the larger-DCS case, and the blue dashed curves are calculated in the smaller-DCS case.

HC, and drying in the subtropical mid-troposphere is due to the strengthening of the descending branch.

The right column of Figure 3 shows the zonal wind changes in different experiments. When DCS increases, the subtropical westerly jet, the trade winds, and the equatorial low-level easterly strengthening are likely a result of the enhanced baroclinicity (equator-to-pole temperature gradient) and HC intensification, which enhances poleward momentum transport. The averaged easterlies

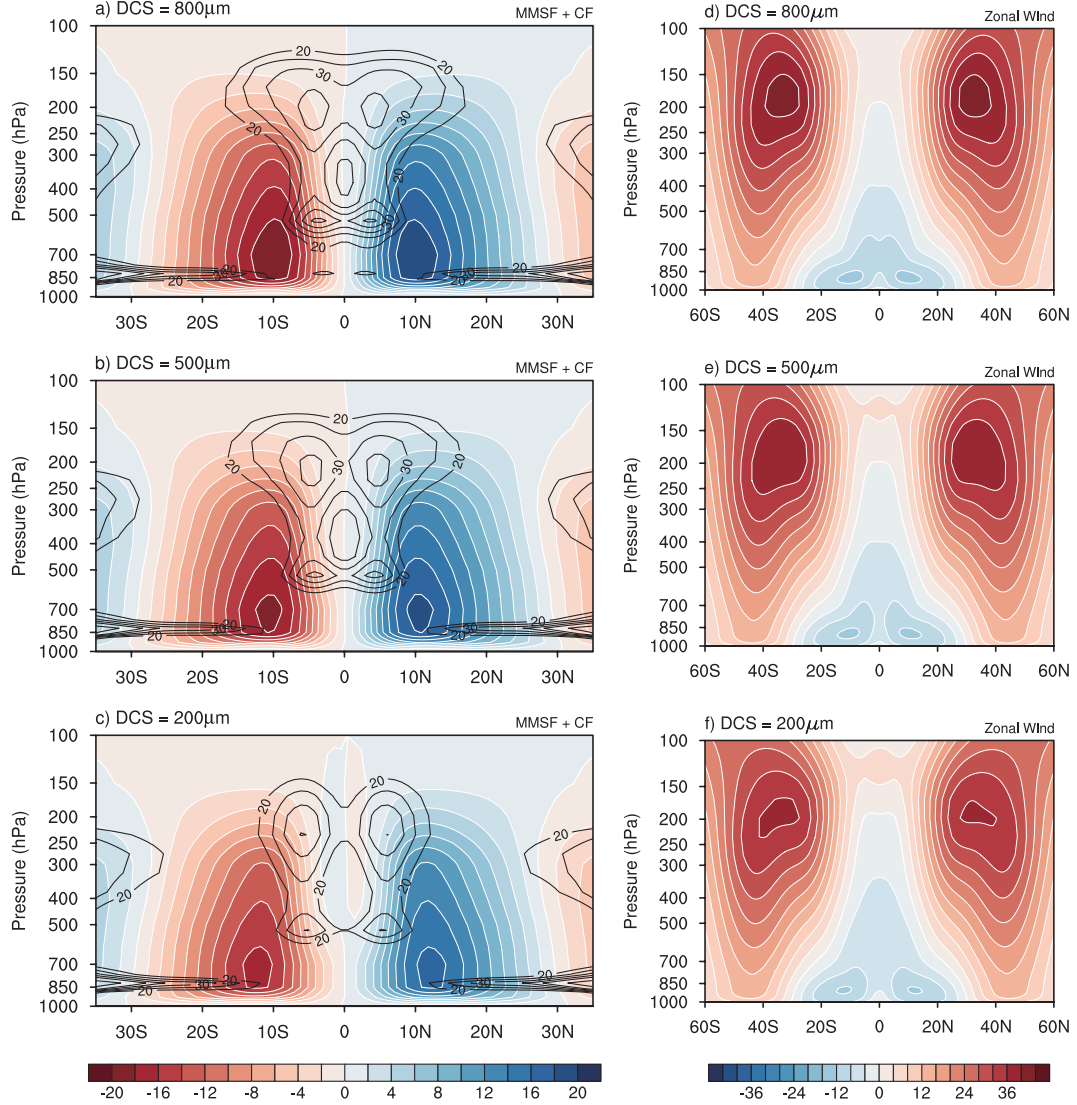


FIG. 3. The climatological zonal-averaged (a, b, c) meridional mass stream function (MMSF, color, units:  $10^{10}$  kg/s) and cloud fraction (contour, units: %), and (d, e, f) zonal wind (units: m/s). The positive MMSF represents the clockwise circulation, while the negative MMSF represents the counter-clockwise circulation. The interval of the cloud fraction contour is not evenly spaced (20, 25, 30, 35, 40, 50, 60).

below 700-hPa within  $5^{\circ}\text{S}$ – $5^{\circ}\text{N}$  are 7.76 m/s, 6.90 m/s, and 5.18 m/s for the simulations of DCS800, DCS500, and DCS200, respectively. Different from the observational equatorial low-level winds with a westerly component over the Warm Pool, the low-level equatorial winds in our aquaplanet simulations are easterlies at all longitudes (figure not shown).

## b. Forcings Causing the Changes

In the tropical atmosphere, diabatic heating primarily arises from two major sources: atmospheric radiative heating and condensational heating. Tuning the DCS parameter directly alters the cloud-radiative effect, which can be represented by the changes in cloud forcing in Figure 4a. The cloud forcing significantly increases in the tropics with DCS, leading to stronger cloud radiative heating. To be specific, the deep-tropical ( $5^{\circ}\text{S}$ – $5^{\circ}\text{N}$ ) averaged cloud forcing is  $16.94 \text{ W/m}^2$ ,  $29.41 \text{ W/m}^2$ , and  $34.16 \text{ W/m}^2$  for DCS200, DCS500, and DCS800, respectively. It increases by 101.7 % from DCS200 to DCS800. The tropical atmosphere is heated by CRI intensification, which may contribute to the changes in tropical temperature and its meridional gradient in Figure 2. Meanwhile, the strengthened HC (Figure 3) is associated with the enhanced meridional temperature gradient and stronger meridional heat transport since HC is a thermal-driven overturning circulation. The study of Bischoff and Schneider (2016) and that of Harrop and Hartmann (2016) suggest that the stronger HC occurs when the equatorial energy input is larger, consistent with our results. It is worth noting that the atmospheric mean state, diabatic forcings, and other climate systems are all coupled, and the changes in HC can also feedback to the cloud forcing and temperature changes.

However, cloud forcing cannot be zonally symmetric. Thus, it should be made clear that the changes in Figure 4a are introduced by changing the clouds of individual convection systems, which collectively change the mean state of the atmosphere.

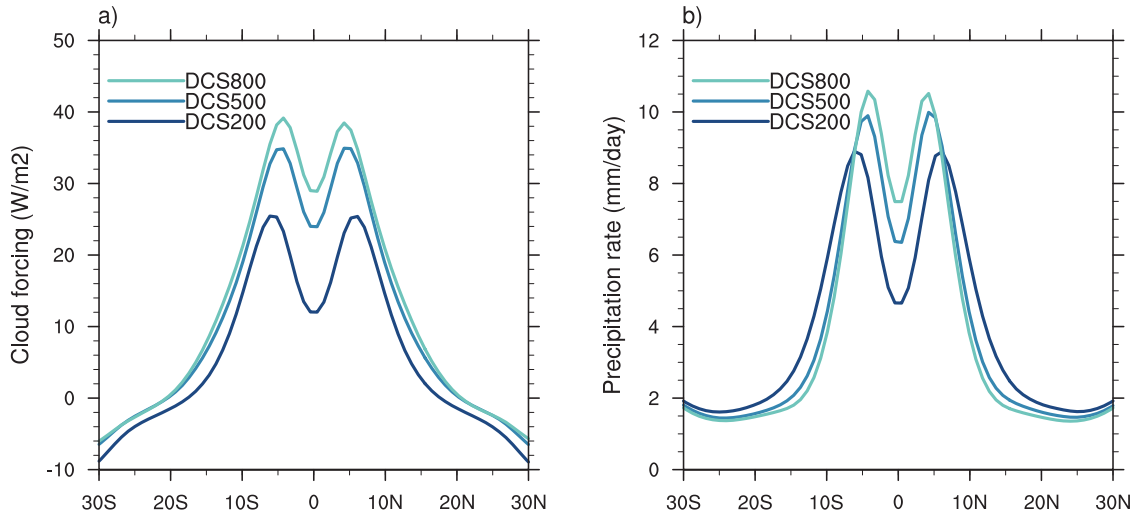


FIG. 4. The climatological zonal-averaged (a) total (LW + SW) cloud forcing (units:  $\text{W/m}^2$ ), and (b) precipitation rate (units:  $\text{mm/day}$ ). Positive cloud forcing values indicate radiative heating.

Figure 4b shows the climatological latitudinal precipitation distribution. By tuning DCS larger, the precipitation increases in the deep tropics with two peaks on both sides of the equator, exhibiting a stronger and narrower ITCZ. Further calculation shows that the averaged precipitation rate within  $5^{\circ}\text{S}$ – $5^{\circ}\text{N}$  is 6.17 mm/day, 8.18 mm/day, 9.19 mm/day for DCS200, DCS500, and DCS800, respectively, increasing by 48.9 % from DCS200 to DCS800. The location and the strength of ITCZ are closely related to the HC changes (Ceppi et al. 2013; Bischoff and Schneider 2016). In our simulations, the stronger and equatorward HC shift corresponds well to the ITCZ changes. The strengthened HC enhances dynamical conditions for ITCZ and the increased radiative heating as well as moisture amount also directly provides the thermodynamic conditions. Due to the coupling of HC and ITCZ, the ITCZ interacts with HC, and its change also provides feedback to HC. As to the displacement of ITCZ, the equatorward contraction of maximum zonal mean convective available potential energy (CAPE) may account for ITCZ contraction (figure not shown), which is associated with the changes in temperature and moisture responding to the CRI changes according to Harrop and Hartmann (2016). The general circulation changes like the contraction of HC can also influence the ITCZ displacement. Similar results are found by Harrop and Hartmann (2016), who suggest that ITCZ contracts toward the equator and the precipitation in the deep tropics increases when turning on the CRI.

To show more details of the changes in the distributions of cloud forcing and precipitation within the tropics, and to better understand the role of DCS, Figure 5a presents the probability density function (PDF) of tropical cloud forcing. We can see that the changes in tropical cloud forcing with DCS mainly show a higher frequency of large cloud forcing events, especially the part larger than  $100 \text{ W/m}^2$ . It seems that the increased probability of large cloud forcing dominantly accounts for the mean cloud forcing changes while the weak cloud forcing has less contribution. As to the changes in tropical precipitation PDF distribution, Figure 5b shows that the median of probability shifts to the heavier precipitation in the tropics with the increasing DCS. The enhanced CRI leads to the increased probability of heavy precipitation and decreased probability of weak precipitation. The extremely large values do not dominate the mean precipitation changes due to the probability being more concentrated in its median, following a log-normal distribution-like pattern.

The joint PDF in Figure 5c–e illustrates the changes in the radiation-precipitation (R-P) relation. This cloud forcing and precipitation do not follow a linear relationship, exhibiting an “S” shape

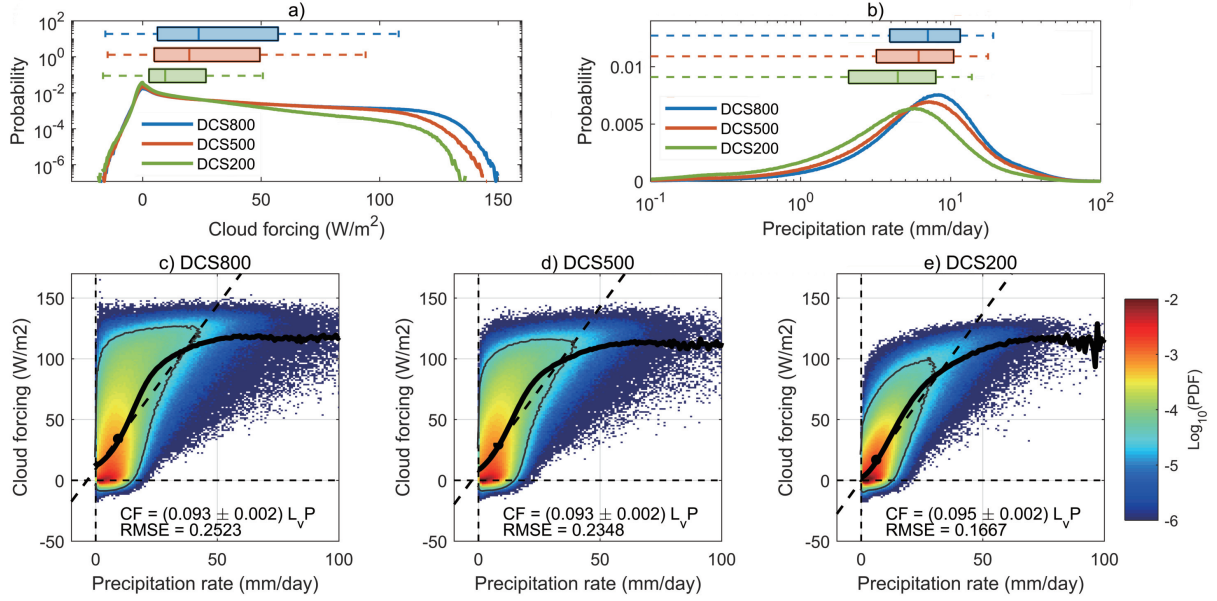


FIG. 5. The comparison of probability density function (PDF) of (a) tropical (5°S–5°N) total cloud radiative forcing (units: W/m²) and tropical precipitation rate (units: mm/day) for different DCS cases. The y-axis in (a) and the x-axis in (b) are on a log scale. Boxplots of different DCS cases are shown over the PDF curves. The left and right edges of the box indicate the 25th and 75th percentiles. The vertical lines in the boxes are the median. The whiskers extend to a maximum of  $1.0 \times$  interquartile range beyond the boxes. (c, d, e) The joint PDF of tropical precipitation rate (units: mm/day) and tropical cloud forcing (units: W/m²) with varying DCS. The probability density is scaled by  $\log_{10}$ . The black dots correspond to the mean precipitation rate and mean cloud forcing. The black dashed lines indicate the linear regression of all colored bins. The thick black solid lines indicate the averaged cloud forcing binned by precipitation rate. The value of gray contours is  $-4.5$ , representing the region of relatively high probability density.

(refer to the black solid curves in joint PDF plots). Near the median (black dots), the cloud forcing increases very fast with the precipitation increase. If we perform a linear regression between cloud forcing and precipitation rate within the gray contour of  $\log_{10}(\text{PDF}) = -4.5$ , the slopes are 0.106, 0.113, and 0.116 for DCS200, DCS500, and DCS800 respectively. The slopes are unitless since the units of precipitation are set to watts per square meter by multiplying the latent heat of vaporization  $L_v$ . Obviously, the slope increases from DCS200 to DCS800, which means the cloud forcing grows faster with increasing precipitation, leading to a stronger cloud-radiative effect per unit precipitation.

303 However, if the linear regression is performed among all colored bins, the slope from DCS200  
304 to DCS800 does not change much (decreases from 0.095 to 0.093), which is contributed by the  
305 fact that the cloud forcing saturates when precipitation becomes very strong. The cloud forcing  
306 distribution can not further grow when precipitation increases with the strongest cloud forcing  
307 being limited below  $150 \text{ W/m}^2$ .

308 We still notice that the highest probability density regions with dark red are located at the lower  
309 left of black dots, away from the mean values. In spite of the lighter red color with the increasing  
310 DCS, the highest probability density regions do not have significant shifts following the shift of  
311 mean values. Accordingly, the black dot becomes farther away from the red region, and the  
312 probability density distribution becomes more dispersed, leading to larger variability.

313 Based on the analyses of Figure 5 above, the changes in cloud forcing can be partially reflected  
314 in the non-linear R-P relation changes. Although the R-P relation does not change substantially,  
315 the probability density of cloud forcing distributes more towards the regions with extremely large  
316 values in all rainfall ranges, making the “S” shape have a larger curvature with increasing DCS.  
317 Nonetheless, the cloud forcing can not grow infinitely with the precipitation increase. It also  
318 reflects that increasing CRI intensity by tuning DCS has limits, especially when DCS is extremely  
319 large.

320 The large cloud forcing is likely associated with deep convection or the stratiform region of the  
321 convective systems, which can be inferred from the statistical relationship between cloud forcing  
322 and precipitation (black solid lines in Figure 5c–e). If we separate the LW and SW components of  
323 cloud forcing (figure not shown), it is obvious that the large cloud forcing mainly comes from the  
324 LW component which is often associated with high clouds. It is understandable because we adjust  
325 the only process related to cloud ice. Cloud ice changes mainly occur in the cold upper troposphere  
326 where the deep convection can reach.

327 In our simulations, the changes in cloud forcing are firstly caused by the varying cloud micro-  
328 physical processes through the DCS tuning. Larger DCS delays snow generation until ice particles  
329 grow to a larger size and thereby keep more cloud ice in the atmosphere. The increased cloud ice  
330 induces stronger CRI, strengthening the cloud forcing but with an upper limit. Consequently, the  
331 mean cloud forcing changes.

On the other hand, the changes in cloud forcing could be partially attributed to the mean state changes: warming and moistening of the tropical atmosphere strengthen HC, favorable for the development of deep convection in the tropical atmosphere and the generation of convective clouds. The increased cloud cover results in stronger cloud forcing, which, in turn, provides feedback to the mean state. This establishes a cloud-radiative-circulation feedback mechanism.

## 4. MJO Responses to CRI Changes

### *a. MJO Characteristics Changes*

The Wheeler-Kiladis wavenumber-frequency spectra (Wheeler and Kiladis 1999, hereafter WK99) of tropical precipitation are shown in Figure 6 to qualitatively measure the scale and strength of convectively coupled equatorial waves. In our aquaplanet simulations, the Kelvin wave-like disturbances are weak with relatively slow propagation speed compared to other models and observations. The relatively broad meridional SST structure in our simulations may account for these differences. Though the power of westward-propagating waves shows some changes with the increasing DCS, the convectively coupled equatorial Rossby (ER) waves seem not distinguishable from the background power. As to other tropical waves like tropical depression (TD)-type waves, mixed Rossby-gravity (MRG) waves, and inertio-gravity (IG) waves, they are also not significant in the spectra of our aquaplanet simulations (some of them are not shown).

Apart from those tropical waves simply discussed above, the most significant power exists within the “MJO band” (eastward propagation; wavenumber one to three; period of 20 to 100 days) in the WK99 spectra, peaking at wavenumber one. In both the symmetric and normalized (symmetric/background) spectra, MJO-like signal power extends to higher wavenumbers and shifts to lower frequencies with increasing DCS. The growth of higher-wavenumber signals may imply a smaller horizontal scale.

To see the frequency changes more clearly, we averaged the power of wavenumber one to three and fit the resulting power-frequency relation to a third-order polynomial around the intraseasonal time scale. For the fitting of the symmetric spectra (Figure 7a), the peak periods are 45, 41, and 34 days for the simulations of DCS800, DCS500, and DCS200, respectively. The stronger CRI associated with larger DCS indeed leads to slower propagation of MJO-like mode. Similar period changes can be also found in the fitting of normalized spectra (Figure 7b).



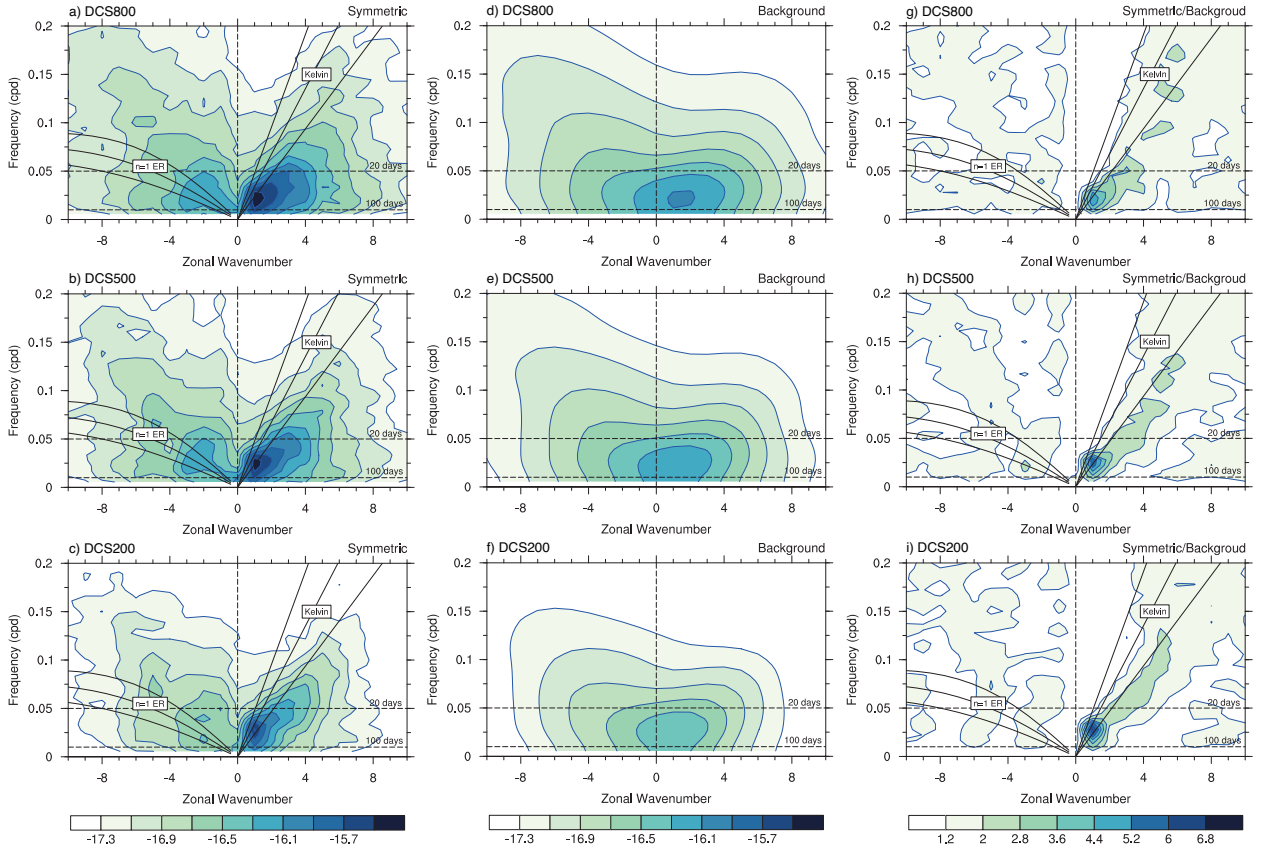


FIG. 6. The Wheeler-Kiladis wavenumber-frequency spectra of precipitation rate within 5°S–5°N: (a, b, c) the symmetric spectra, (d, e, f) the background spectra, and (g, h, i) the normalized spectra (symmetric power divided by background power). The symmetric spectra and background are scaled by  $\log_{10}$ . The superimposed black solid lines are the dispersion curves. The temporal window length is 180 days, and the overlapping temporal segments are 90 days.

It is quite interesting that the power at wavenumber one in the symmetric and normalized spectra responds differently as the CRI intensity changes. The signals within the MJO band in the normalized spectra become weaker when DCS is larger, but the opposite trend exists in symmetric spectra. Such significant difference, rarely found and discussed in previous studies, needs attention and emphasis. When DCS increases, the stronger power within the MJO band in the symmetric spectra shows a stronger intensity of MJO-like mode, as the precipitation increases in this spatiotemporal scale. The stronger eastward-propagating low-frequency signal power with the increasing DCS in the background spectra (Figure 6d–f) can explain the weaker MJO signals

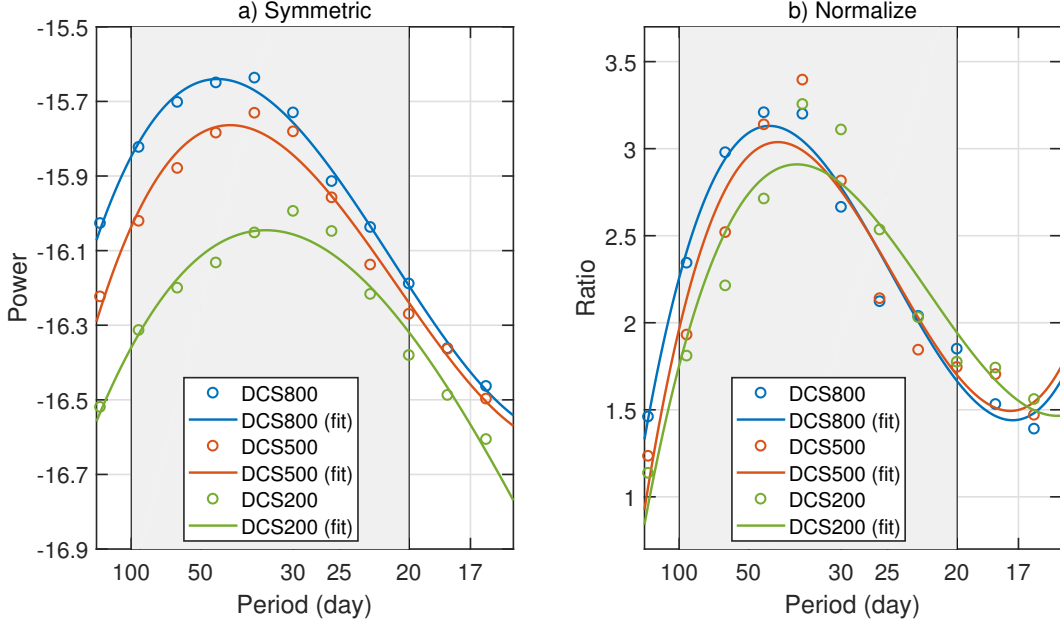


FIG. 7. (a) The tropical ( $5^{\circ}\text{S}$ – $5^{\circ}\text{N}$ ) precipitation power (averaged within wavenumber 1–3) changes with period (1/frequency, units: day) and their polynomial fitting curves based on the symmetric spectra in Figure 6. The periods at the maximum fitted power are 44.64 days, 41.15 days, and 34.13 days, corresponding to DCS800, DCS500, and DCS200, respectively. The power in the y-axis is scaled by  $\log_{10}$ . (b) The ratio (averaged within wavenumber 1–3) changes with the period and their polynomial fitting curves based on the normalized spectra in Figure 6. The periods at the maximum fitted ratio are 43.48 days, 41.32 days, and 37.04 days, corresponding to DCS800, DCS500, and DCS200 respectively.

in the normalized spectra. It means that the MJO-like signals become less prominent and more indistinguishable compared to the background, rather than suggesting a weaker MJO-like wave.

It seems that the DCS-induced CRI changes not only influence the MJO-like waves but also influence the waves in other scales, as shown by the growth of precipitation power in symmetric spectra. The changes in other-scale waves contribute to the mean state changes. Meanwhile, the waves in different scales have interactions and energy transfer (c.f., Wallace et al. 2023), also influencing the representation of MJO-like signals and their scale selection. Therefore, the relatively less prominent MJO-like signals with increasing DCS are possibly influenced by the changes in other waves.

In the regression maps (Figure 8), all fields represent approximate wavenumber one spatial structure centering at  $(0^{\circ}, 180^{\circ})$  where the positive precipitation anomalies (left column) and the

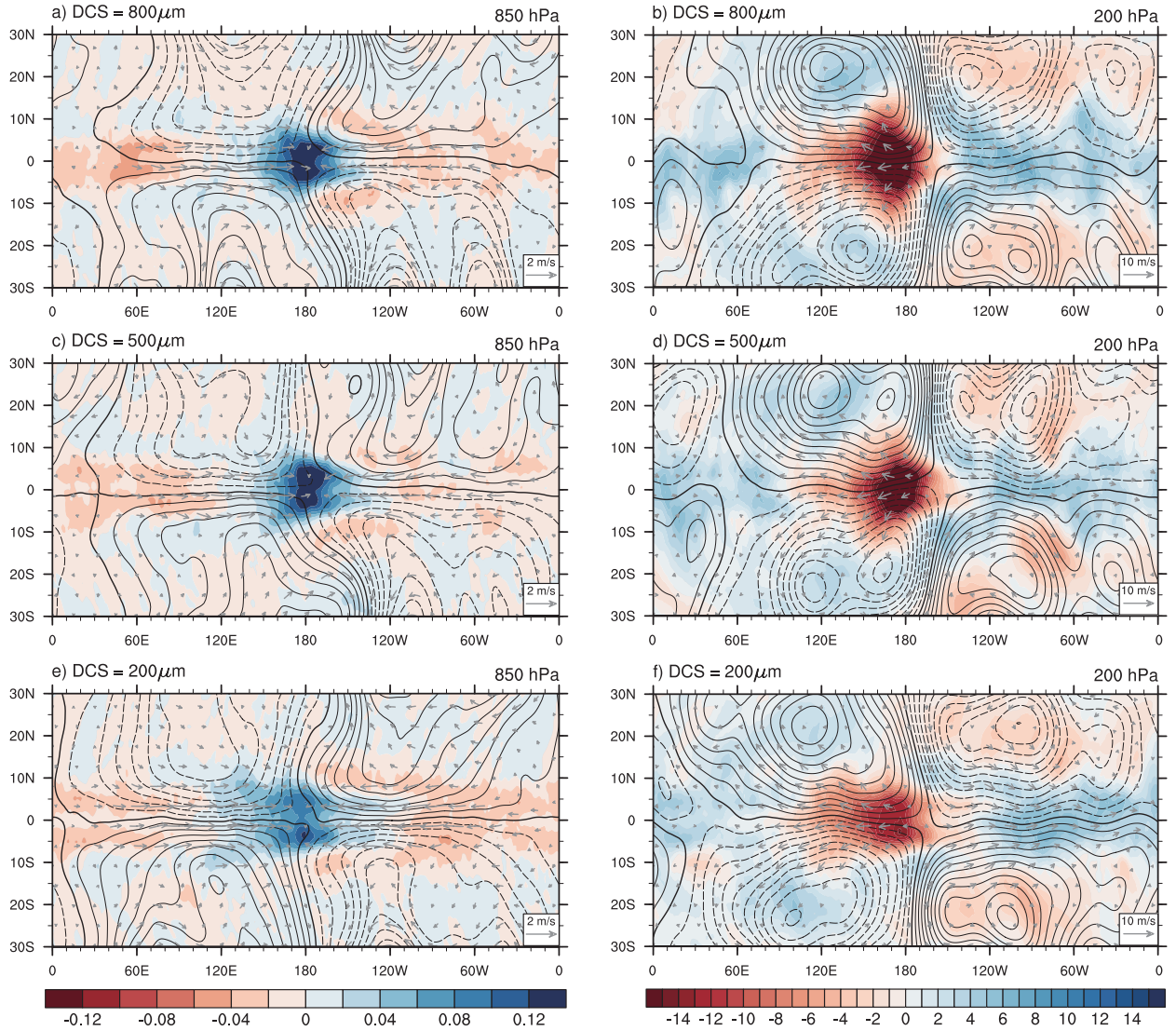


FIG. 8. The regression of (a, c, e) precipitation rate (color, units: mm/hr), (b, d, f) OLR (color, units:  $\text{W}/\text{m}^2$ ), wind (vector, units: m/s), and stream function (contour, units:  $10^6 \text{ m}^2/\text{s}$ ) onto the MJO index. For wind and stream function, the left column is at approximate 850-hPa, and the right column is at approximate 200-hPa. Dashed contours indicated negative values. Contour intervals for stream function at 850-hPa and 200-hPa are  $0.2 \times 10^6 \text{ m}^2/\text{s}$  and  $0.5 \times 10^6 \text{ m}^2/\text{s}$ , respectively.

negative OLR (right column) anomalies are at maximum amplitudes. The regressed precipitation fields exhibit weak “swallowtail” shapes to the west of heavy precipitation centers, consistent with the observational MJO (Zhang and Ling 2012; Adames and Wallace 2015). From the low-level wind fields and stream function fields (left column), it is apparent that the CESM2 aquaplanet model

401 can well produce the poleward anomalous flows to the east of convective centers and the wind-  
402 convection coupling in 850-hPa without phase differences, superior to some simulations (Zhang  
403 2005; Shi et al. 2018) that simulate the unrealistic poleward flows or unrealistic convergence to the  
404 west of convective centers. The high-level wind and stream function in the right column of Figure  
405 8 also shows relatively reasonable wind-convection coupling compared to the observational MJO.  
406 With the increasing DCS, the wind vectors near the convective centers show a stronger poleward  
407 anomalous transport, indicating a stronger divergence corresponding with the stronger convection.

408 As for how CRI effects manifest in the horizontal structure of MJO-like mode, the enhancement  
409 of precipitation and OLR anomalies at the convective center with the increasing DCS can be seen  
410 in Figure 8. Less LW radiation escaping into space means more radiative heating results from  
411 the high-level cloud increase. The heavier rainfall and more intense radiative heating imply that  
412 the MJO convection intensifies and the MJO precipitation variance increases. In addition, when  
413  $DCS = 200 \mu m$ , the flow field is dominated by wavenumber one, showing a more stable and  
414 broader structure than other cases, and the "swallowtail" shape in the precipitation field has a wider  
415 zonal span. Higher-wavenumber disturbances (especially the structure of wavenumber 2–3), by  
416 contrast, appear in the flow fields when DCS increases; meanwhile, the "swallowtail" shape shrinks  
417 zonally with shorter tails or even disappears. The emergence of higher-wavenumber signals and  
418 the smaller-scale patterns are consistent with the implications from the WK99 spectra (Figure 6),  
419 likely associated with the enhancement of convection in all scales due to the mean state changes.

420 The vertical structure of MJO-like mode in our simulations is also shown in the regression maps  
421 (Figure 9). We make an average over the deep tropical region ( $5^{\circ}S$ – $5^{\circ}N$ ), and similar features  
422 can be obtained if the range is expanded to  $10^{\circ}S$ – $10^{\circ}N$ . In the intraseasonal scale, the positive  
423 cloud fraction anomalies increase at the convective center in the mid- and upper-troposphere  
424 (shading in Figure 9a–b). More clouds are produced in the larger-DCS experiments, leading to  
425 the stronger MJO-associated cloud forcing, which can be inferred from the cloud radiative heating  
426 rate anomalies (contour in Figure 9d–f). The radiative heating associated with clouds deducts the  
427 clearsky component for removing the radiative heating induced by moisture. Its anomalies at the  
428 convective centers show significant increases below the high clouds and extend to higher levels  
429 with the increasing DCS.

430 The temperature vertical cross sections (shading in Figure 9d–f) exhibit pronounced positive  
 431 anomalies at the convective center above the middle troposphere with negative anomalies aloft  
 432 and below, showing “boomerang”-like shapes, consistent with the observational MJO (Adames  
 433 and Wallace 2014b). The stronger temperature positive anomalies with DCS may come from the  
 434 changes in radiative heating, latent heating, and advection around the MJO centers. It seems like  
 435 the warmer higher-level troposphere tends to reduce the buoyancy and weaken the instability, while  
 436 the stronger low-level moisture convergence with the increasing DCS (figure not shown) provides  
 437 the moisture and dynamics forces for supporting stronger convection, which overcomes the reduced  
 438 potential of free convection induced by the weakened buoyancy.

445 The mass flux vector in Figure 9a–c measures how the air mass transports vertically. It can be  
 446 regarded as resolved mass flux, but not the parameterized convective mass flux. In the DCS200  
 447 case (Figure 9c), the mass flux has a relative upright updraft at 180° longitude, while the mass flux  
 448 gradually tilts westward with height as the DCS increases with longer arrows, showing a stronger  
 449 vertical transport and a stronger mass divergence above the mid-troposphere. It is also evidence  
 450 supporting the strengthening of MJO convection.

451 Another quantity often used in MJO studies is moist static energy (MSE), also referred to as  
 452 frozen MSE. It is denoted by  $h$ , and defined as

$$h = C_p T + gZ + L_v q - L_f q_i, \quad (3)$$

453 where  $C_p$  is the specific heat at constant pressure,  $T$  is the temperature,  $g$  is the gravitational  
 454 acceleration,  $Z$  is the height,  $L_v$  is the latent heat of vaporization,  $q$  is the specific humidity of  
 455 water vapor,  $L_f$  is the latent heat of sublimation and  $q_i$  is the specific quantity of ice. The MSE is  
 456 conserved in moist adiabatic processes.

457 The vertical regression of MSE associated with MJO is also shown in Figure 9a–c. At the MJO  
 458 convective centers, the MSE exhibits positive anomalies in most tropospheric atmosphere, peaking  
 459 at around 500-hPa. When DCS is larger, MSE positive anomalies increase, especially in the  
 460 middle troposphere. It means that more energetic weather systems can generate, also confirming  
 461 the MJO-intensification.

462 To sum up, the most pronounced changes in the characteristics of MJO-like mode associated with  
 463 the increasing CRI are 1) intensification, 2) slower propagation, and 3) smaller zonal scale. Such a

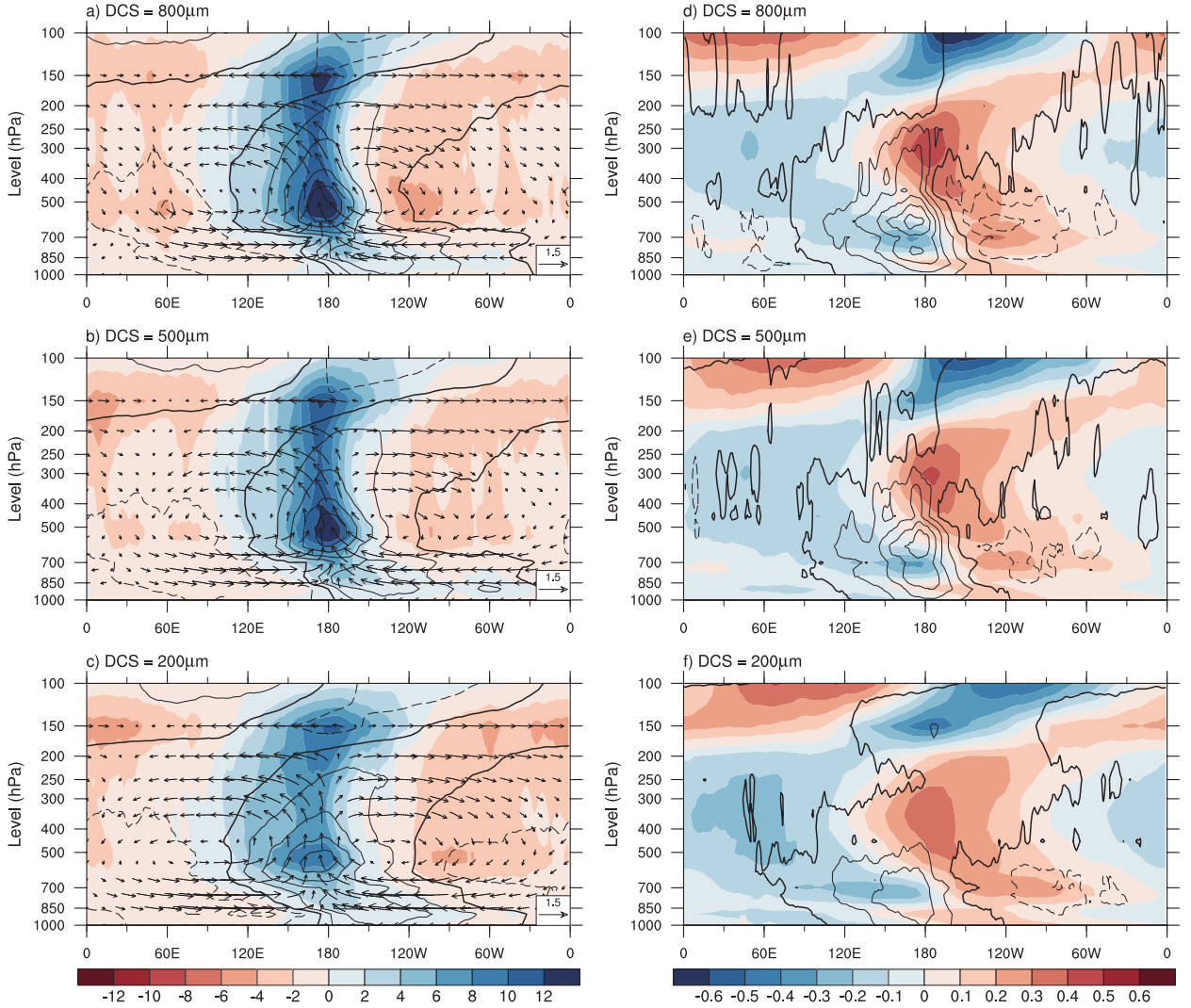


FIG. 9. (a, b, c) The vertical regression of cloud fraction (color, units: %), moist static energy (MSE, contour, units:  $10^2 \text{ J m}^{-2}$ ), and mass flux ( $\rho u$  and  $\rho w$ , vector, units:  $\text{kg m}^{-2} \text{ s}^{-1}$ ) within  $5^{\circ}\text{S}$ – $5^{\circ}\text{N}$  onto the MJO index. (d, e, f) As in (a, b, c), except the regressed quantities are air temperature (color, units:  $^{\circ}\text{C}$ ) and total (LW + SW) cloud radiative heating rate (contour, units: K/day). The dashed contour indicates negative values. The contour interval for MSE is  $3 \times 10^2 \text{ J m}^{-2}$  and for radiative heating rate is 0.05 K/day.  $\rho w$  is multiplied by a factor of 250.

simulated space-time relationship is consistent with the observational results of Lyu et al. (2021)’s study, which suggests a broader extension of MJO is associated with a faster propagation, and vice versa. In the following analysis, we mainly focus on the mechanisms of MJO intensification and slower propagation.

468 *b. Physical Processes Causing the Changes*

469 1) MSE MAINTENANCE AND PROPAGATION

470 The general consensus of previous studies suggests the importance of moisture in MJO mecha-  
 471 nisms. To better understand the MJO-like mode's maintenance and propagation, we can infer the  
 472 key processes from the MSE budget analysis.

473 The mass-weighted column-integrated MSE is the integral of MSE from the bottom to the top  
 474 of the atmospheric column as follows:

$$\langle h \rangle = \int_{p_{\text{top}}}^{p_{\text{sfc}}} h \frac{dp}{g}, \quad (4)$$

475 where  $\langle \dots \rangle$  represents the mass-weighted vertical integral,  $p$  is the pressure,  $p_{\text{sfc}}$  is the surface  
 476 pressure and  $p_{\text{top}}$  is the pressure at the top of model. The other column-integrated variables all  
 477 follow this equation.

478 The column-integrated MSE tendency can be expressed in the budget style:

$$\left\langle \frac{\partial h}{\partial t} \right\rangle = -\left\langle \omega \frac{\partial h}{\partial p} \right\rangle - \langle \mathbf{V} \cdot \nabla h \rangle + LH + SH + \langle LW \rangle + \langle SW \rangle, \quad (5)$$

479 where  $\mathbf{V}$  is the horizontal wind vector on a pressure level,  $\nabla$  is the gradient operator,  $\omega$  is the  
 480 pressure velocity,  $LH$  and  $SH$  are the latent heat flux and the sensible heat flux from the surface  
 481 into the atmospheric column, and the  $\langle LW \rangle$  and  $\langle SW \rangle$  are the column-integrated LW and SW  
 482 radiative heating rates. The term on the left of Equation 5 is the local  $\langle h \rangle$  tendency (MSE tendency  
 483 term), where the daily data is used for calculating the tendency. On the right of Equation 5, the  
 484 first term is column-integrated vertical advection of  $h$  (vertical advection term), the second term  
 485 is column-integrated horizontal advection of  $h$  (horizontal advection term) and the rest four terms  
 486 are the heating sources. The residual term is calculated as the differences between the directly  
 487 calculated  $\langle \partial h / \partial t \rangle$  and the sum of six budget terms to the right of Equation 5, representing the  
 488 numerical errors.

489 The patterns of column-integrated MSE anomalies and column-integrated MSE tendency anoma-  
 490 lies associated with MJO are shown in Figure 10. The upper row of Figure 10 exhibits positive  
 491 MSE anomalies at the MJO center with the two dry anomalous regions on both sides of the east



492 and west. This pattern is similar to the precipitation and OLR fields in Figure 8, also reflecting the  
493 basic spatial structure of MJO-like mode. The column MSE anomalies at the MJO center increase  
494 from DCS200 to DCS800 generally, while the DCS500 case seems to exhibit higher maximum  
495 values. It is somewhat surprising but reasonable and the results of the following MSE budget  
496 analysis won't be affected much.

497 If we look at the regressed MSE vertical distribution (Figure 9a–c), we can find that the stronger  
498 negative MSE anomalies in the upper troposphere account for the smaller column-integrated MSE  
499 in DCS800 compared to DCS500. According to the definition of MSE (Equation 3), MSE is  
500 determined by temperature, height, and moisture. Among the three quantities (the figures related  
501 to the geopotential height and moisture anomalies are not shown), only the temperature provides  
502 negative contributions to the MSE changes in the upper troposphere, as shown by the cooling  
503 anomalies near the tropopause in Figure 9d–f. In fact, the cooling anomalies are centered in the  
504 stratosphere (not shown). When DCS increases, the cooling anomalies become stronger. We  
505 speculate that the stronger cooling anomalies may be attributed to two aspects. First, the stronger  
506 CRI with more clouds in the upper troposphere traps the anomalous heating within the troposphere,  
507 preventing upwelling radiative flux to the stratosphere over the convective centers. Second, the CRI  
508 changes may also influence the waves in the stratosphere which can interact with the tropospheric  
509 atmosphere. However, it is beyond the scope of our study.

510 In the lower row of Figure 10, the distribution of MJO-regressed column MSE tendency shows  
511 approximately a quarter phase difference ahead of column MSE. The MSE tendency has positive  
512 anomalies to the east of the convective center with negative anomalies to the west. The config-  
513 uration of MSE and its tendency anomalies determines the eastward propagation of MJO. When  
514 CRI intensifies, the zonal range of strong tropical MSE tendency anomalies shrinks toward the  
515 convective center (the estimation of the zonal range is described in the caption of Figure 10) and  
516 the amplitude of tropical MSE tendency anomalies becomes lower (the amplitude can be estimated  
517 by the difference of the maximum positive and negative MSE tendency anomalies around the  
518 convective center within 5°S–5°N). The local MSE changes with time become slower when DCS  
519 increases, implying a slower propagation of MJO-like mode, consistent with our previous results.  
520 We also notice that the MSE tendency anomalies in DCS200 peak on the equator, while double



peaks straddling the equator occur in DCS500 and DCS800. The vertical advection anomaly changes (Figure A1d–f) mainly contribute to it.

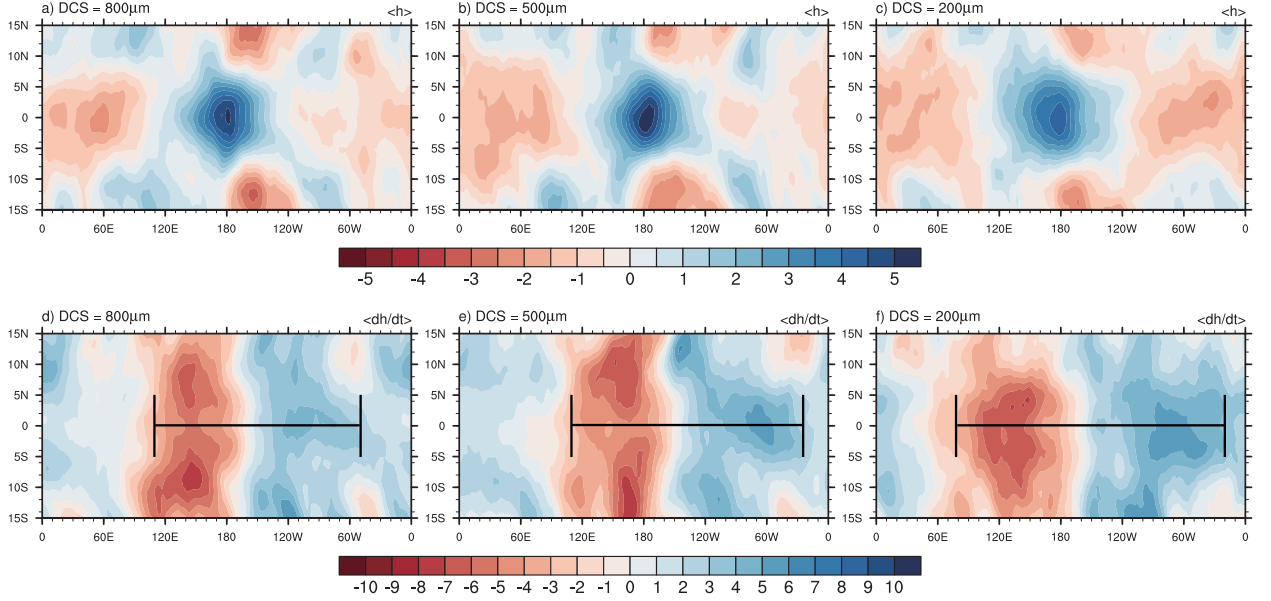


FIG. 10. The regression of (a, b, c) column-integrated MSE (units:  $10^6 \text{ J/m}^2$ ) and (d, e, f) column-integrated MSE tendency (units:  $10^5 \text{ J m}^{-2} \text{ day}^{-1}$ ) onto the MJO index. The width of the thick black lines estimates the zonal range of the strong tropical MSE tendency anomalies around the convective center. The ends to both sides of the black lines are located at the contour equal to around  $\pm 4 \times 10^5 \text{ J m}^{-2} \text{ day}^{-1}$ .

To examine how the MSE budget terms contribute to the maintenance and propagation of MJO-like mode, we follow the projecting method proposed by Andersen and Kuang (2012). Figure 11 illustrates the calculation results which are the fractional contributions of MJO-regressed MSE budget terms to the MJO-regressed column MSE and MSE tendency. They can be calculated as

$$S_m(x) = \frac{\|x \cdot \langle h \rangle\|}{\|\langle h \rangle^2\|}, \quad (6)$$

$$S_p(x) = \frac{\|x \cdot \langle \partial h / \partial t \rangle\|}{\|\langle \partial h / \partial t \rangle^2\|}, \quad (7)$$

where  $S_m$  and  $S_p$  represent the projection onto the maintenance and propagation respectively,  $x$  is MJO-regressed MSE budget term,  $\|y\| = \int \int y dA$  is the integral of  $y$  over the deep tropics  $A$  ( $5^\circ\text{S}$ – $5^\circ\text{N}$ , all longitudes). If we enlarge the integral region to  $10^\circ\text{S}$ – $10^\circ\text{N}$ , similar results are obtained. The sum of six projection terms is named “total” in Figure 11. The differences between

“total” and the MSE tendency term are due to the existence of the residual term. Although the residual term is not small enough to be ignored, it does not affect our qualitative analysis of other terms.

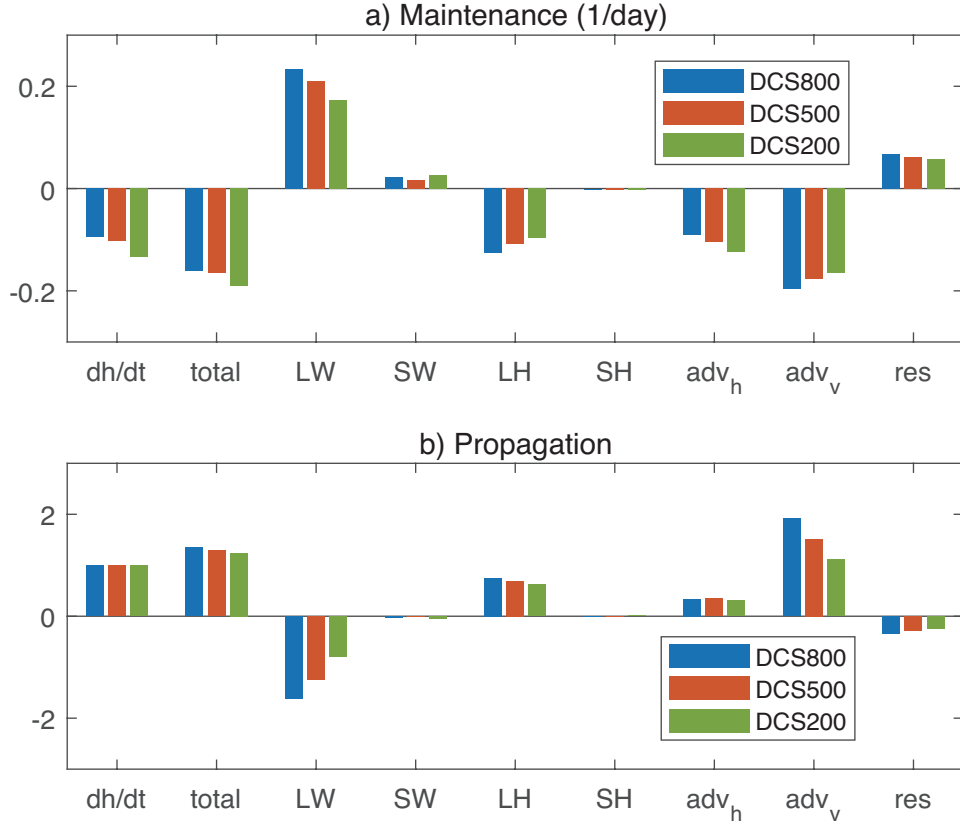


FIG. 11. The projection of MSE budget terms onto the MJO-regressed (a) column MSE and (b) column MSE tendency. The MJO-regressed fields used for projection calculation are all longitudes within 5°S–5°N.

In Figure 11a, the column MSE tendency  $\langle \partial h / \partial t \rangle$  has a negative contribution to the MSE maintenance. The opposite phases between MSE anomalies and MSE tendency anomalies (shown in Figure 10) account for the negative contribution. In the convective center of MJO-like mode, the column MSE tends to export, showing negative MSE tendency anomalies. When DCS increases, the negative contribution of  $\langle \partial h / \partial t \rangle$  reduces, meaning a reduced MSE export. The anomalous MSE import maintains the MJO-like mode.

As we can see from Figure 11, the LW radiation term is distinguishable from other sources, contributing to the maintenance of column MSE and slowing down its eastward propagation. The SW radiation term has the same effect, however, its contribution is not significant. Regarding the

two terms as total radiative heating source, the MSE budget bar chart obviously highlights the role of CRI in MJO-like mode. When DCS increases, the CRI has a larger positive contribution to the maintenance and a larger negative contribution to the propagation. It is the only term among the MSE budget terms that is well consistent with the characteristic changes of the MJO-like mode, intensifying the MJO-like mode and retarding its eastward propagation with the increasing DCS.

The horizontal and vertical advection terms are the sink for maintaining the column MSE (Figure 11a), which is consistent with the results in Andersen and Kuang (2012). The advection terms show different phases compared to the column MSE anomalies (Figure 10a–c), with negative advection (both for horizontal and vertical advection) anomalies at the convective centers (Figure A1a–c and Figure A1d–f). It implies that the MSE tends to export from the air column, especially exporting MSE in the high levels due to the strong outflow if the convection is mature. Thus, the convection is strong at the MJO convective centers but tends to dissipate, showing a negative contribution to its maintenance. When DCS increases, the role of horizontal advection in dissipation weakens, while the role of vertical advection strengthens. The opposite changes in response to the DCS increases make their effects offset each other and make their total effect insignificant in MJO changes.

For the MJO propagation (Figure 11b), the advection terms are the source of eastward propagation, especially the vertical advection term with the largest contribution. When DCS increases, the contribution of horizontal advection to the propagation barely changes. Instead, the vertical advection term exhibits much more significant changes with the increasing DCS, accelerating MJO's eastward propagation. Such acceleration effect is opposite to our simulation results, meaning that the role of the vertical advection must be overcome by other factors. Among the six budget terms, only the LW radiation term can provide a completely opposite effect against vertical advection. This result further demonstrates that the CRI dominates the slower propagation of MJO-like mode in our simulations, although the role of MSE advection associated with the column MSE convergence or divergence can not be neglected. In some sense, the vertical advection and LW terms should be combined as they both come from the same process (convection).

The surface latent heat flux (SLHF) anomalies associated with the wind-induced surface heat exchange (WISHE) feedback are often regarded as an important driver for the destabilization of MJO, even more dominant than the CRI (e.g., Fuchs and Raymond 2017; Jiang et al. 2020). However, the LH term does not seem a dominant contribution to the MSE budget in Figure 11,

and the negative contribution of the LH term to the MJO maintenance is against the previous understanding of the role of WISHE feedback. In our simulations, the negative SLHF anomalies associated with MJO-like mode occur within and to the west of the convective centers and the positive SLHF anomalies occur to the east (Figure A1g–i), which is almost opposite to the phase of column MSE anomalies (Figure 10a–c), accounting for the negative contribution. Such a distribution of SLHF anomalies is unlike (even opposite to) the observed distribution which shows positive SLHF anomalies within and to the west of the MJO convective center and negative SLHF anomalies to the east, at least over the Warm-Pool longitudes (Jones and Weare 1996; Gao et al. 2019; Sentić et al. 2020). Given that our simulations provide a uniform equatorial easterly mean state unlike the westerlies over the Warm Pool, the disparity of the role of LH term in the MJO maintenance between our simulations and the observations is likely attributed to the mean state wind differences.

To summarize the MSE budget analysis, it confirms the crucial role of CRI in changing MJO-like mode in our simulations. The maintenance and propagation changes in MJO-like mode are dominantly determined by CRI, though other processes, such as the low-level moisture convergence, are also important to MJO-like mode. When DCS increases, more clouds with more cloud ice are generated and persist longer at the convective center in the intraseasonal scale, producing stronger radiative heating there (dominated by the LW radiative heating). The stronger radiative heating anomalies in air columns appear in phase with the column MSE positive anomalies, acting as a dominant energy source for the maintenance of MJO-like mode. Thus, the MJO-like mode tends to intensify and generate more precipitation under the stronger CRI. CRI intensification also decelerates the MJO-like mode, which is mainly because of the phase difference between the LW radiative heating and the MSE tendency (Figure A1j–l and Figure 10), manifesting as the LW radiative heating center lagging behind the positive MSE tendency center.

## 2) INFERENCES FROM MEAN STATE CHANGES

The CRI not only influences the MJO behavior directly in the intraseasonal scale but also likely influences MJO through the DCS-induced mean state changes.

In Section 3, we find that the DCS-induced CRI intensification warms and moistens the tropics (Figure 2), meanwhile causing a strengthened HC (Figure 3). The changed CRI and atmospheric

mean state stimulate cloud-radiative-circulation feedback, which provides favorable conditions for the development of deep convection and generation of convective clouds in the tropics, consistent with the precipitation power changes in the symmetric and background WK99 spectra (Figure 6). In those spectra, we can see the power intensifies almost in all spatial-temporal scales.

MJO is an organized convective system traveling in the tropics. In such an environment conducive to convection, MJO is more likely to generate stronger convection and precipitation. As shown in the symmetric WK99 spectra, the power signal within the MJO band becomes stronger as the signals in other scales do. It can be regarded as a pathway that the mean state change influences MJO.

What's more, the subtropical mid-troposphere dries as we increase DCS (Figure 2d-f). This enhances meridional moisture gradient, and might further accelerate MJO propagation based on Kang et al. (2021), who discuss the MJO propagation over the Maritime Continent in boreal winter. However, the changes in MJO propagation in our simulations are inconsistent with Kang et al. (2021). Our idealized simulations without zonal asymmetry, seasonal cycle, and land-sea distribution may partially account for this discrepancy, which is worth further investigation.

## 5. Summary and Discussion

This study investigates how CRI affects tropical mean state and MJO-like mode by tuning a sensitive cloud microphysics parameter (DCS) in the CESM2 aquaplanet model. The findings suggest that DCS-induced CRI changes play a crucial role in altering the mean state and modulating the MJO characteristics.

Increasing DCS results in changes in cloud properties, leading to more high clouds with a stronger CRI. It greatly changes the tropical mean state by increasing the tropospheric temperature and moisture in the tropics, increasing the meridional heat and moisture gradient, as well as strengthening the Hadley circulation and trade winds. The tropical precipitation and cloud radiative forcing are also enhanced under the CRI intensification. On the one hand, the mean state changes in our simulations can be explained by the direct role of cloud microphysics parameterization changes. On the other hand, the mean state changes with CRI can be also elucidated from the so-called cloud-radiative-circulation feedback. The DCS-induced mean state changes create a favorable environment for deep convection, generating more convective clouds. The CRI, thereby,

638 can be also strengthened via cloud-radiative-circulation feedback, which is a different pathway  
639 from the manual parameter tuning.

640 The unique role of DCS in cloud forcing and precipitation is also examined from the probability  
641 density function. Increasing DCS strongly affects the extreme cloud forcing (larger than  $100 \text{ W/m}^2$ ),  
642 and shifts the median of precipitation PDF to a heavier precipitation range. As to the relationship  
643 between them (call it R-P relation), it exhibits a non-linear “S” shape. If the cloud forcing and  
644 precipitation are near the median, the cloud forcing grows faster with increasing precipitation when  
645 DCS is larger, leading to a stronger cloud-radiative effect per unit precipitation. However, the cloud  
646 forcing saturates when precipitation is very strong, which indicates that the cloud forcing has its  
647 limit and the effect of tuning DCS is also limited when the DCS value is over a reasonable range.

648 The DCS-induced CRI changes can also influence the MJO-like mode characterized by eastward  
649 propagation, wavenumber-1 features, and a 20-100-day period. With the strengthened CRI, the  
650 MJO-like mode intensifies with a stronger precipitation power in WK99 symmetric spectra and  
651 propagates more slowly with a lower frequency. However, the MJO-like signals are more difficult  
652 to be distinguished from the background possibly due to the stronger background precipitation and  
653 the influence of other waves.

654 According to the MSE budget analysis, the CRI, especially the LW radiative forcing, directly  
655 influences MJO on the intraseasonal scale, dominating its intensity and propagation changes. With  
656 the increasing DCS, LW radiative heating has a larger positive contribution to MJO maintenance and  
657 a larger negative contribution to MJO eastward propagation. As to other terms in the MSE budget,  
658 some of them offset each other, some of them barely change, and some of them are overcome  
659 by the radiation term. The role of CRI can be also explained as follows: when strengthening  
660 CRI, more clouds, more precipitation, stronger radiative heating, stronger upward motion, and  
661 larger MSE in the middle troposphere are diagnosed at the MJO convective center, supporting the  
662 intensification of MJO-like mode. The phase difference between LW radiative heating and MSE  
663 tendency accounts for the deceleration.

664 The CRI not only influences MJO directly through the adjustment between radiation and con-  
665 vection on the intraseasonal scale but also influences MJO through the DCS-induced mean state  
666 changes. The mean state changed by CRI intensification provides a warmer, moister tropical

667 atmosphere with stronger HC, beneficial to the tropical convection in all spatial-temporal scales,  
668 including the convection within “MJO band” shown in WK99 spectra.

669 We note the special method that simply uses the DCS parameter to control the CRI. It provides  
670 a novel perspective for considering the effects of CRI. However, the DCS parameter behaves with  
671 different values in different models (Zhang et al. 2013; Fan et al. 2021) and is chosen arbitrarily  
672 (Eidhammer et al. 2014) due to no physical and observational basis (Eidhammer et al. 2017).  
673 Efforts are underway to address this uncertainty. It may be worth exploring the realistic conditions  
674 under which DCS can increase to establish a connection between DCS and the real world before  
675 new approaches replace the “auto-conversion” in parameterization schemes.

676 Although we mainly focus on the significant role of CRI when discussing the changes in MJO-  
677 like mode, it does not mean that other processes are not important to MJO, especially the WISHE  
678 feedback. In fact, which mechanism, CRI or WISHE, determines MJO has not been well answered  
679 yet and lacks consensus (e.g., Jiang et al. 2020). As discussed in Section 4b, we observe the  
680 disparity of the WISHE effect on MJO between our aquaplanet simulations with an equatorial  
681 low-level easterly mean state and the observations with equatorial westerlies over the Warm Pool.  
682 In this study, we do not discuss too much on the WISHE feedback due to the unrealistic mean  
683 state induced possibly unrealistic SLHF anomalies. Nevertheless, how do the mean state winds  
684 influence the intraseasonal variabilities? When MJO propagates eastward passing through the  
685 Maritime Continent and perhaps undergoing a transition between different mean wind states, how  
686 does the role of WISHE change? More studies are still needed on these questions.

*Acknowledgments.* We greatly appreciate the comments and suggestions from the three anonymous reviewers. The work described in this paper was substantially supported by a grant from the Research Grants Council of the Hong Kong Special Administrative Region, China (Project Reference Number: AoE/P-601/23-N) and the Center for Ocean Research in Hong Kong and Macau (CORE), a joint research center between the Laoshan Laboratory and Technology and the Hong Kong University of Science and Technology (HKUST). The supercomputer Tianhe-2 used for computation is provided by National Supercomputer Center in Guangzhou, China. DK was supported by New Faculty Startup Fund from Seoul National University, NASA MAP program (80NSSC21K1495), NOAA MAPP program (NA21OAR4310343), NOAA CVP program (NA22OAR4310608), and KMA R&D program (KMI2021-01210)

*Data availability statement.* The CESM2 model can be accessed from the official website (<https://www.cesm.ucar.edu/models/cesm2/>). Due to the substantial data size, cloud-storage for our simulation data is inconvenient. For inquiries about accessing our simulation data, please contact us for sharing.

## APPENDIX

### MSE Budget Terms

The MSE budget terms are regressed onto the MJO index before calculating the their fractional contribution to the MJO maintenance and propagation. Four main terms (horizontal advection term, vertical advection term, LH term, and LW radiation term) with the significant contributions are shown in Figure A1.

### References

- Adames, Á. F., and J. M. Wallace, 2014a: Three-Dimensional Structure and Evolution of the MJO and Its Relation to the Mean Flow. *Journal of the Atmospheric Sciences*, **71** (6), 2007–2026, <https://doi.org/10.1175/JAS-D-13-0254.1>.
- Adames, Á. F., and J. M. Wallace, 2014b: Three-Dimensional Structure and Evolution of the Vertical Velocity and Divergence Fields in the MJO. *Journal of the Atmospheric Sciences*, **71** (12), 4661–4681, <https://doi.org/10.1175/JAS-D-14-0091.1>.



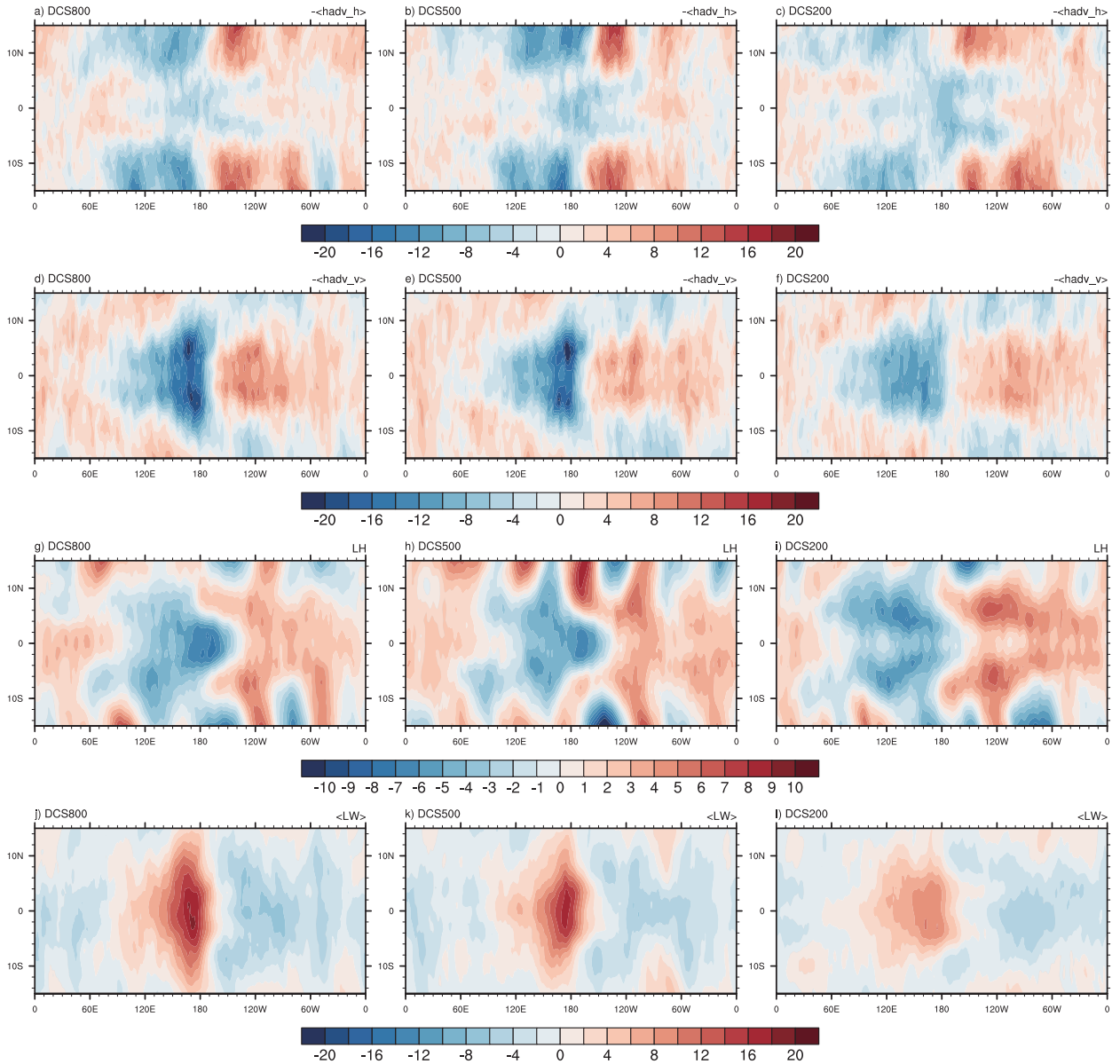


FIG. A1. The regression of different MSE budget terms onto the MJO index: (a, b, c) horizontal advection term, (d, e, f) vertical advection term, (g, h, i) LH term, and (j, k, l) LW radiation term. Units:  $\text{W/m}^2$ .

Adames, Á. F., and J. M. Wallace, 2015: Three-Dimensional Structure and Evolution of the Moisture Field in the MJO. *Journal of the Atmospheric Sciences*, **72** (10), 3733–3754, <https://doi.org/10.1175/JAS-D-15-0003.1>.

Andersen, J. A., and Z. Kuang, 2012: Moist Static Energy Budget of MJO-like Disturbances in the Atmosphere of a Zonally Symmetric Aquaplanet. *Journal of Climate*, **25** (8), 2782–2804,

<https://doi.org/10.1175/JCLI-D-11-00168.1>.

Benedict, J. J., B. Medeiros, A. C. Clement, and J. G. Olson, 2020: Investigating the Role of Cloud-Radiation Interactions in Subseasonal Tropical Disturbances. *Geophysical Research Letters*, **47** (9), <https://doi.org/10.1029/2019GL086817>.

Bischoff, T., and T. Schneider, 2016: The Equatorial Energy Balance, ITCZ Position, and Double-ITCZ Bifurcations. *Journal of Climate*, **29** (8), 2997–3013, <https://doi.org/10.1175/JCLI-D-15-0328.1>.

Bogenschutz, P. A., A. Gettelman, C. Hannay, V. E. Larson, R. B. Neale, C. Craig, and C.-C. Chen, 2018: The path to CAM6: Coupled simulations with CAM5.4 and CAM5.5. *Geoscientific Model Development*, **11** (1), 235–255, <https://doi.org/10.5194/gmd-11-235-2018>.

Ceppi, P., and D. L. Hartmann, 2015: Connections Between Clouds, Radiation, and Midlatitude Dynamics: A Review. *Current Climate Change Reports*, **1** (2), 94–102, <https://doi.org/10.1007/s40641-015-0010-x>.

Ceppi, P., Y.-T. Hwang, X. Liu, D. M. W. Frierson, and D. L. Hartmann, 2013: The relationship between the ITCZ and the Southern Hemispheric eddy-driven jet. *Journal of Geophysical Research: Atmospheres*, **118** (11), 5136–5146, <https://doi.org/10.1002/jgrd.50461>.

Ceppi, P., M. D. Zelinka, and D. L. Hartmann, 2014: The response of the Southern Hemispheric eddy-driven jet to future changes in shortwave radiation in CMIP5. *Geophysical Research Letters*, **41** (9), 3244–3250, <https://doi.org/10.1002/2014GL060043>.

Crueger, T., and B. Stevens, 2015: The effect of atmospheric radiative heating by clouds on the Madden-Julian Oscillation. *Journal of Advances in Modeling Earth Systems*, **7** (2), 854–864, <https://doi.org/10.1002/2015MS000434>.

Eidhammer, T., H. Morrison, A. Bansemer, A. Gettelman, and A. J. Heymsfield, 2014: Comparison of ice cloud properties simulated by the Community Atmosphere Model (CAM5) with in-situ observations. *Atmospheric Chemistry and Physics*, **14** (18), 10 103–10 118, <https://doi.org/10.5194/acp-14-10103-2014>.

747 Eidhammer, T., H. Morrison, D. Mitchell, A. Gettelman, and E. Erfani, 2017: Improvements in  
 748 Global Climate Model Microphysics Using a Consistent Representation of Ice Particle Properties.  
 749 *Journal of Climate*, **30** (2), 609–629, <https://doi.org/10.1175/JCLI-D-16-0050.1>.

750 Fan, Y., Y. T. Chung, and X. Shi, 2021: The Essential Role of Cloud-Radiation Interaction in Non-  
 751 rotating Convective Self-Aggregation. *Geophysical Research Letters*, **48** (19), e2021GL095 102,  
 752 <https://doi.org/10.1029/2021GL095102>.

753 Fuchs, Ž., and D. J. Raymond, 2002: Large-Scale Modes of a Nonrotating Atmosphere with  
 754 Water Vapor and Cloud–Radiation Feedbacks. *Journal of the Atmospheric Sciences*, **59** (10),  
 755 1669–1679, [https://doi.org/10.1175/1520-0469\(2002\)059<1669:LSMOAN>2.0.CO;2](https://doi.org/10.1175/1520-0469(2002)059<1669:LSMOAN>2.0.CO;2).

756 Fuchs, Z., and D. J. Raymond, 2005: Large-Scale Modes in a Rotating Atmosphere with Radiative–  
 757 Convective Instability and WISHE. *Journal of the Atmospheric Sciences*, **62** (11), 4084–4094,  
 758 <https://doi.org/10.1175/JAS3582.1>.

759 Fuchs, Ž., and D. J. Raymond, 2017: A simple model of intraseasonal oscillations. *Journal of Ad-  
 760 vances in Modeling Earth Systems*, **9** (2), 1195–1211, <https://doi.org/10.1002/2017MS000963>.

761 Fuchs-Stone, Ž., 2020: WISHE-Moisture Mode in a Vertically Resolved Model. *Journal  
 762 of Advances in Modeling Earth Systems*, **12** (2), e2019MS001 839, [https://doi.org/10.1029/  
 763 2019MS001839](https://doi.org/10.1029/2019MS001839).

764 Gao, Y., P.-C. Hsu, and T. Li, 2019: Effects of high-frequency activity on latent heat flux of MJO.  
 765 *Climate Dynamics*, **52** (3-4), 1471–1485, <https://doi.org/10.1007/s00382-018-4208-1>.

766 Gettelman, A., and H. Morrison, 2015: Advanced Two-Moment Bulk Microphysics for Global  
 767 Models. Part I: Off-Line Tests and Comparison with Other Schemes. *Journal of Climate*, **28** (3),  
 768 1268–1287, <https://doi.org/10.1175/JCLI-D-14-00102.1>.

769 Golaz, J.-C., V. E. Larson, and W. R. Cotton, 2002: A PDF-Based Model for Boundary Layer  
 770 Clouds. Part I: Method and Model Description. *Journal of the Atmospheric Sciences*, **59** (24),  
 771 3540–3551, [https://doi.org/10.1175/1520-0469\(2002\)059<3540:APBMFB>2.0.CO;2](https://doi.org/10.1175/1520-0469(2002)059<3540:APBMFB>2.0.CO;2).

772 Harrop, B. E., and D. L. Hartmann, 2016: The Role of Cloud Radiative Heating in Determining  
 773 the Location of the ITCZ in Aquaplanet Simulations. *Journal of Climate*, **29** (8), 2741–2763,  
 774 <https://doi.org/10.1175/JCLI-D-15-0521.1>.

775 Hu, Q., Z. Han, and S. Wang, 2022: Cloud Radiative Effects on MJO Development in DYNAMO.  
776 *Journal of Climate*, **35** (21), 6969–6984, <https://doi.org/10.1175/JCLI-D-21-0882.1>.

777 Iacono, M. J., J. S. Delamere, E. J. Mlawer, M. W. Shephard, S. A. Clough, and W. D. Collins,  
778 2008: Radiative forcing by long-lived greenhouse gases: Calculations with the AER radiative  
779 transfer models. *Journal of Geophysical Research: Atmospheres*, **113** (D13), [https://doi.org/](https://doi.org/10.1029/2008JD009944)  
780 10.1029/2008JD009944.

781 Jiang, X., and Coauthors, 2020: Fifty Years of Research on the Madden-Julian Oscillation:  
782 Recent Progress, Challenges, and Perspectives. *Journal of Geophysical Research: Atmospheres*,  
783 **125** (17), <https://doi.org/10.1029/2019JD030911>.

784 Jones, C., and B. C. Weare, 1996: The Role of Low-Level Moisture Convergence and Ocean  
785 Latent Heat Fluxes in the Madden and Julian Oscillation: An Observational Analysis Using  
786 ISCCP Data and ECMWF Analyses. *Journal of Climate*, **9** (12), 3086–3104, [https://doi.org/](https://doi.org/10.1175/1520-0442(1996)009<3086:TROLLM>2.0.CO;2)  
787 10.1175/1520-0442(1996)009<3086:TROLLM>2.0.CO;2.

788 Kang, D., D. Kim, M.-S. Ahn, and S.-I. An, 2021: The Role of the Background Meridional  
789 Moisture Gradient on the Propagation of the MJO over the Maritime Continent. *Journal of*  
790 *Climate*, **34** (16), 6565–6581, <https://doi.org/10.1175/JCLI-D-20-0085.1>.

791 Kim, D., M.-S. Ahn, I.-S. Kang, and A. D. Del Genio, 2015: Role of Longwave Cloud–Radiation  
792 Feedback in the Simulation of the Madden–Julian Oscillation. *Journal of Climate*, **28** (17),  
793 6979–6994, <https://doi.org/10.1175/JCLI-D-14-00767.1>.

794 Larson, V. E., J.-C. Golaz, and W. R. Cotton, 2002: Small-Scale and Mesoscale Variability in  
795 Cloudy Boundary Layers: Joint Probability Density Functions. *Journal of the Atmospheric*  
796 *Sciences*, **59** (24), 3519–3539, [https://doi.org/10.1175/1520-0469\(2002\)059<3519:SSAMVI>2.](https://doi.org/10.1175/1520-0469(2002)059<3519:SSAMVI>2.0.CO;2)  
797 0.CO;2.

798 Lee, M.-I., I.-S. Kang, J.-K. Kim, and B. E. Mapes, 2001: Influence of cloud-radiation interaction  
799 on simulating tropical intraseasonal oscillation with an atmospheric general circulation model.  
800 *Journal of Geophysical Research: Atmospheres*, **106** (D13), 14 219–14 233, [https://doi.org/](https://doi.org/10.1029/2001JD900143)  
801 10.1029/2001JD900143.

- 802 Leroux, S., and Coauthors, 2016: Inter-model comparison of subseasonal tropical variability in  
 803 aquaplanet experiments: Effect of a warm pool. *Journal of Advances in Modeling Earth Systems*,  
 804 **8** (4), 1526–1551, <https://doi.org/10.1002/2016MS000683>.
- 805 Li, Y., D. W. J. Thompson, and S. Bony, 2015: The Influence of Atmospheric Cloud Radiative  
 806 Effects on the Large-Scale Atmospheric Circulation. *Journal of Climate*, **28** (18), 7263–7278,  
 807 <https://doi.org/10.1175/JCLI-D-14-00825.1>.
- 808 Lyu, M., X. Jiang, Z. Wu, D. Kim, and Á. F. Adames, 2021: Zonal-Scale of the Madden-Julian  
 809 Oscillation and Its Propagation Speed on the Interannual Time-Scale. *Geophysical Research*  
 810 *Letters*, **48** (6), e2020GL091 239, <https://doi.org/10.1029/2020GL091239>.
- 811 Madden, R. A., and P. R. Julian, 1971: Detection of a 40–50 Day Oscillation in the Zonal Wind  
 812 in the Tropical Pacific. *Journal of the Atmospheric Sciences*, **28** (5), 702–708, [https://doi.org/10.1175/1520-0469\(1971\)028<0702:DOADOI>2.0.CO;2](https://doi.org/10.1175/1520-0469(1971)028<0702:DOADOI>2.0.CO;2).
- 814 Maloney, E. D., A. H. Sobel, and W. M. Hannah, 2010: Intraseasonal variability in an aquaplanet  
 815 general circulation model. *Journal of Advances in Modeling Earth Systems*, **2**, 5, <https://doi.org/10.3894/JAMES.2010.2.5>.
- 817 Medeiros, B., A. C. Clement, J. J. Benedict, and B. Zhang, 2021: Investigating the impact of cloud-  
 818 radiative feedbacks on tropical precipitation extremes. *npj Climate and Atmospheric Science*,  
 819 **4** (1), 1–10, <https://doi.org/10.1038/s41612-021-00174-x>.
- 820 Medeiros, B., D. L. Williamson, and J. G. Olson, 2016: Reference aquaplanet climate in the  
 821 Community Atmosphere Model, Version 5. *Journal of Advances in Modeling Earth Systems*,  
 822 **8** (1), 406–424, <https://doi.org/10.1002/2015MS000593>.
- 823 Morrison, H., and A. Gettelman, 2008: A New Two-Moment Bulk Stratiform Cloud Microphysics  
 824 Scheme in the Community Atmosphere Model, Version 3 (CAM3). Part I: Description and Nu-  
 825 merical Tests. *Journal of Climate*, **21** (15), 3642–3659, <https://doi.org/10.1175/2008JCLI2105.1>.
- 826 Pathak, R., S. Sahany, and S. K. Mishra, 2020: Uncertainty quantification based cloud parame-  
 827 terization sensitivity analysis in the NCAR community atmosphere model. *Scientific Reports*,  
 828 **10** (1), 17 499, <https://doi.org/10.1038/s41598-020-74441-x>.

- Rushley, S. S., D. Kang, D. Kim, S.-I. An, and T. Wang, 2023: MJO in Different Orbital Regimes: Role of the Mean State in the MJO's Amplitude during Boreal Winter. *Journal of Climate*, **36** (13), 4475–4490, <https://doi.org/10.1175/JCLI-D-22-0725.1>.
- Sentić, S., Ž. Fuchs-Stone, and D. J. Raymond, 2020: The Madden-Julian Oscillation and Mean Easterly Winds. *Journal of Geophysical Research: Atmospheres*, **125** (10), <https://doi.org/10.1029/2019JD030869>.
- Shaw, T. A., 2019: Mechanisms of Future Predicted Changes in the Zonal Mean Mid-Latitude Circulation. *Current Climate Change Reports*, **5** (4), 345–357, <https://doi.org/10.1007/s40641-019-00145-8>.
- Shi, X., D. Kim, Á. F. Adames, and J. Sukhatme, 2018: WISHE-Moisture Mode in an Aquaplanet Simulation. *Journal of Advances in Modeling Earth Systems*, **10** (10), 2393–2407, <https://doi.org/10.1029/2018MS001441>.
- Sobel, A., and E. Maloney, 2012: An Idealized Semi-Empirical Framework for Modeling the Madden–Julian Oscillation. *Journal of the Atmospheric Sciences*, **69** (5), 1691–1705, <https://doi.org/10.1175/JAS-D-11-0118.1>.
- Tao, W.-K., S. Lang, J. Simpson, C.-H. Sui, B. Ferrier, and M.-D. Chou, 1996: Mechanisms of Cloud-Radiation Interaction in the Tropics and Midlatitudes. *Journal of the Atmospheric Sciences*, **53** (18), 2624–2651, [https://doi.org/10.1175/1520-0469\(1996\)053<2624:MOCRII>2.0.CO;2](https://doi.org/10.1175/1520-0469(1996)053<2624:MOCRII>2.0.CO;2).
- Tian, B., and V. Ramanathan, 2003: A Simple Moist Tropical Atmosphere Model: The Role of Cloud Radiative Forcing. *Journal of Climate*, **16** (12), 2086–2092, [https://doi.org/10.1175/1520-0442\(2003\)016<2086:ASMTAM>2.0.CO;2](https://doi.org/10.1175/1520-0442(2003)016<2086:ASMTAM>2.0.CO;2).
- Wallace, J. M., D. S. Battisti, D. W. J. Thompson, and D. L. Hartmann, 2023: The Atmospheric General Circulation. Cambridge University Press, <https://doi.org/10.1017/9781108563857>.
- Wheeler, M., and G. N. Kiladis, 1999: Convectively Coupled Equatorial Waves: Analysis of Clouds and Temperature in the Wavenumber–Frequency Domain. *Journal of the Atmospheric Sciences*, **56** (3), 374–399, [https://doi.org/10.1175/1520-0469\(1999\)056<0374:CCEWAO>2.0.CO;2](https://doi.org/10.1175/1520-0469(1999)056<0374:CCEWAO>2.0.CO;2).

856 Williamson, L., and Coauthors, 2012: The APE atlas. <https://doi.org/10.5065/D6FF3QBR>.

857 Zhang, B., R. J. Kramer, and B. J. Soden, 2019: Radiative Feedbacks Associated with the  
858 Madden–Julian Oscillation. *Journal of Climate*, **32** (20), 7055–7065, [https://doi.org/10.1175/](https://doi.org/10.1175/JCLI-D-19-0144.1)  
859 JCLI-D-19-0144.1.

860 Zhang, B., B. J. Soden, G. A. Vecchi, and W. Yang, 2021: Investigating the Causes and Impacts  
861 of Convective Aggregation in a High Resolution Atmospheric GCM. *Journal of Advances in*  
862 *Modeling Earth Systems*, **13** (11), e2021MS002675, <https://doi.org/10.1029/2021MS002675>.

863 Zhang, C., 2005: Madden-Julian Oscillation. *Reviews of Geophysics*, **43** (2), [https://doi.org/](https://doi.org/10.1029/2004RG000158)  
864 10.1029/2004RG000158.

865 Zhang, C., and J. Ling, 2012: Potential Vorticity of the Madden–Julian Oscillation. *Journal of the*  
866 *Atmospheric Sciences*, **69** (1), 65–78, <https://doi.org/10.1175/JAS-D-11-081.1>.

867 Zhang, G. J., and N. A. McFarlane, 1995: Sensitivity of climate simulations to the parameterization  
868 of cumulus convection in the Canadian climate centre general circulation model. *Atmosphere-*  
869 *Ocean*, **33** (3), 407–446, <https://doi.org/10.1080/07055900.1995.9649539>.

870 Zhang, K., X. Liu, M. Wang, J. M. Comstock, D. L. Mitchell, S. Mishra, and G. G. Mace, 2013:  
871 Evaluating and constraining ice cloud parameterizations in CAM5 using aircraft measurements  
872 from the SPARTICUS campaign. *Atmospheric Chemistry and Physics*, **13** (9), 4963–4982,  
873 <https://doi.org/10.5194/acp-13-4963-2013>.

874 Zhao, C., and Coauthors, 2013: A sensitivity study of radiative fluxes at the top of atmo-  
875 sphere to cloud-microphysics and aerosol parameters in the community atmosphere model  
876 CAM5. *Atmospheric Chemistry and Physics*, **13** (21), 10 969–10 987, [https://doi.org/10.5194/](https://doi.org/10.5194/acp-13-10969-2013)  
877 acp-13-10969-2013.